Journal of Materials Processing Technology 213 (2013) 2217–2237

Contents lists available at ScienceDirect

Journal of Materials Processing Technology

journal homepage: www.elsevier.com/locate/jmatprotec

# Determination of tool friction in presence of flank wear and stress distribution based validation using finite element simulations in machining of titanium and nickel based alloys

Durul Ulutan, Tuğrul Özel*

*Manufacturing & Automation Research Laboratory, Industrial and Systems Engineering, Rutgers University, NJ 08854, USA*

ARTICLE INFO

*Article history:*
Received 10 April 2013
Accepted 23 May 2013
Available online 3 June 2013

*Keywords:*
Machining
Friction
Tool edge radius
Stagnation point
Titanium alloys
Nickel-based alloys

ABSTRACT

Tool friction plays a very important role in machining titanium and nickel-based alloys and is an important parameter in Finite Element based machining simulations. It is the source for the high amount of heat generation, and as a result, the excessive flank wear during machining these materials. The worn tool is known to create poor surface qualities with high tensile surface residual stresses, machining induced surface hardening, and undesirable surface roughness. It is essential to develop a methodology to determine how and to what extent the friction is built up on the tool. This study facilitates a determination methodology to estimate the stress distributions on the rake and flank surfaces of the tool and resultant friction coefficients between the tool and the chip on tool rake face, and the tool and the workpiece on tool flank face. The methodology is applied to various tool edge radii and also utilized in solving stagnation point location on the tool edge. Predicted friction results are further validated with comparison of predicted stress distributions from FE simulations for machining of titanium alloy Ti-6Al-4V and the nickel-based alloy IN-100. It was found that tool stresses and friction are mainly influenced by tool rake angle, edge radius, and tool flank wear and are slightly affected by the cutting conditions in the ranges that were considered in this study.



## 1. Introduction

Machining difficult-to-process materials such as titanium and nickel-based alloys has been a major hurdle for manufacturing industry in terms of productivity for a significant amount of time, and there are a number of issues that are yet to be resolved. The effect of friction is an important issue, yet its understanding in machining titanium and nickel-based alloys is not complete. Let alone 3D machining processes, the work on friction in 2D orthogonal machining processes still lacks entirety. It is known that with increasing friction, heat build-up and tool wear increases especially in the case of titanium and nickel-based alloys due to their low thermal conductivity and chemical affinity with tool materials at elevated temperatures. Consequently, there are surface integrity problems at the end product that will reduce product effectiveness, quality and reliability.

While it is extremely important to understand the role of friction, attempts at measuring in situ detailed frictional properties during machining have been a far cry from success. Hence, attempting to get the optimum approximation by modeling friction still remains a tangible approach to this problem. Childs (2006a) reviewed friction laws and models existed in metal cutting and claimed that different friction models should be considered in low, intermediate, and high speed cutting regimes. He also pointed out the limitations of using traditional metal forming based friction models available in Finite Element Modeling software and suggested an improved friction model based on a constant friction coefficient being replaced by one which increases with plastic strain rate. Finite Element-based models comprise the most important part of the modeling work, and it is known that FE-based models are practically used to find optimal cutting conditions and tool geometry parameters. In addition, flow stress characteristics of work material at specified cutting parameters and friction characteristics at tool/chip interface are two important factors that affect FE-based simulation capability and predictability. Özel (2006) investigated several friction models applicable to FE-based simulations of metal cutting and claimed a friction coefficient varying with normal stress provides better predictions of cutting forces and tool stress distributions. Arrazola et al. (2008) showed that a friction coefficient alone is inadequate and does not represent the friction between chip–tool interfaces in metal cutting. They also suggested a variable friction coefficient that is empirically obtained from cutting tests. Arrazola and Özel (2010) investigated the influence of limiting shear stress on the tool–chip contact friction and

* Corresponding author. Tel.: +1 732 445 1099; fax: +1 732 445 5467.
*E-mail address:* ozel@rci.rutgers.edu (T. Özel).

0924-0136/$ – see front matter © 2013 Elsevier B.V. All rights reserved.
http://dx.doi.org/10.1016/j.jmatprotec.2013.05.019

**Nomenclature**

| | |
|---|---|
| $a$-$h_{1-2}$ | coefficients of the non-linear relationships |
| $A$,$B$,$C$,$D$ | FE material model coefficients |
| $m$,$n$,$p$,$r$,$s$ | FE material model coefficients |
| $b$ | depth of cut |
| $c_p$ | specific heat capacity |
| $h$ | heat conduction coefficient |
| $l_c$ | chip–tool contact length along the tool rake face |
| $l_p$ | plastic contact length along the tool rake face |
| $E$ | Young's Modulus |
| $F_c$ | total cutting force |
| $F_f$ | total feed force |
| $F_{c_o}$ | cutting force for the 3rd zone—ploughing or edge components |
| $F_{f_o}$ | feed force for the 3rd zone—ploughing or edge components |
| $F_{n_{1-3}}$ | normal force components |
| $F_{t_{1-3}}$ | tangential force components |
| $F_{n_{1-3c}}$ | cutting force components due to normal stresses |
| $F_{n_{1-3c}}$ | cutting force components due to tangential stresses |
| $F_{n_{1-3f}}$ | feed force components due to normal stresses |
| $F_{n_{1-3f}}$ | feed force components due to tangential stresses |
| $m$ | exponential coefficient for Region III |
| $n$ | exponential coefficient for Region I |
| $r_\beta$ | cutting edge radius |
| $T$ | temperature |
| $T_0$ | ambient temperature |
| $T_m$ | melting temperature |
| $t_u$ | uncut chip thickness |
| $VB$ | tool flank wear length |
| $v_c$ | cutting speed |
| $x_{1-2}$ | distance along the rake and flank faces from edge face |
| $\alpha$ | angle measured from cutting speed direction for Region II |
| $\alpha_0$ | starting angle for Region II |
| $\alpha_f$ | final angle for Region II |
| $\alpha_t$ | thermal expansion constant |
| $\gamma_1$ | rake angle |
| $\gamma_2$ | clearance angle |
| $\gamma_s$ | stagnation point angle |
| $\varepsilon$ | true strain |
| $\dot{\varepsilon}_0$ | reference true strain rate |
| $\dot{\varepsilon}$ | true strain rate |
| $\theta$ | tool flank wear angle |
| $\lambda$ | thermal conduction coefficient |
| $\mu$ | mean friction coefficient |
| $\mu_{ap}$ | apparent friction coefficient |
| $\mu_{sl}$ | sliding friction coefficient |
| $\mu_1$ | friction coefficient along the rake face |
| $\mu_2$ | friction coefficient along the flank face |
| $\sigma$ | flow stress |
| $\sigma_{1-3}$ | normal stress at the rake, edge, and flank faces |
| $\sigma_{1_{max}}$ | maximum normal stress at the rake face |
| $\tilde{\sigma}_2$ | normal stress at the stagnation point in Region II for the worn tool |
| $\sigma_{3_{max}}$ | maximum normal stress at the flank face |
| $\tau_{1-3}$ | shear stress at the rake, edge, and flank faces |
| $\tau_{1_{max}}$ | maximum shear stress along the tool rake face |
| $\tilde{\tau}_2$ | frictional shear stress at the stagnation point in Region II for the worn tool |
| $\tau_{3_{max}}$ | maximum shear stress along the tool flank face |

concluded that friction models that limit the increasing shear stress are more effective in predicting physical variables in metal cutting. Childs (2006b) focused on FE-based simulation and the role of friction models in plastic and elastic–plastic workpiece assumptions to explore the physical limitations of the friction. He claimed that friction stress proportional to normal stress is a tolerable friction law in the FE-based simulations but acknowledged that it is unrealistic in plastically flowing conditions. Meanwhile, other friction models for analytical and semi-empirical machining modeling have been proposed. Özlü et al. (2009) used a friction model that considers both apparent and real contacts exist on tool rake face. They also proposed an experimental method to identify the parameters of such a friction model. Thus, continued attention has been given to friction modeling in literature.

In parallel to those studies, present Finite Element based simulation models for machining nowadays take tool friction at rake and flank faces as an input to the model. In addition, shear friction and sliding friction can be represented together in a "hybrid friction model" at the tool–chip contact for a cutting tool with an edge radius ($r_\beta > 0$). In this model, coexisting friction regions are defined; a shear friction region ($m = \tau/k$, where $\tau$ is material shear stress and $k$ is shear flow stress in the shearing zone) around of the tool edge radius curvature and a sliding region along the rest of the rake face represented with a friction coefficient ($\mu = \tau_f/\sigma_n$, where $\tau_f$ is the friction stress and $\sigma_n$ is the normal stress on the tool face). Similarly friction at the tool–workpiece contact can be represented while the extent of sticking region and friction coefficient in sliding region remaining as major unknowns in metal cutting conditions.

This study will introduce a comprehensive friction determination methodology beginning with measured cutting forces at various cutting conditions, tool geometry, and tool flank wear for machining titanium and nickel-based alloys. Tool contact friction on rake and flank faces will be determined by using an analytical modeling approach and an iterative solution methodology to identify stress distributions and related friction coefficients at those faces for each cutting condition. FE-based simulation modeling working in an iterative algorithm together with the analytical and empirical models will be utilized to validate predicted tool friction coefficients and stress distributions. Particularly, the developed friction models with and without tool wear will be introduced, and their validation with force measurements for force components as well as FE-based model for stress distributions will be shown. The paper will be finalized by suggestions on how to utilize the information and findings of this study for future research.

### 1.1. Friction determination methods

There have been many attempts to determine the friction coefficient during machining, and one should know the strength and weaknesses of all of these methods to propose a new method. Despite being similar to each other in many ways, there are nuances that separate these methods, and it is important to understand these differences.

In the pin-on-the-disk method, a tribometer with a stationary pin is contacted with the rotating disk, measuring the forces. The ratio of the force components gives the coefficient of friction, but the machining temperature and pressure cannot be maintained for the measurement. According to Bonnet et al. (2008), this leads to inaccurate measurements, since the coefficient of friction is considered to be dependent on these factors. In order to achieve machining temperature, Olsson et al. (1989) and later Hedenqvist and Olsson (1991) proposed methods where the pin follows the cutting tool, so the workpiece is still at cutting temperature. They used an improved method that also imitates the cutting pressure and measured forces very similar to machining forces. In their method, Bonnet et al. (2008) coated the pin with the tool material, which

rubs the surface of the disk, where a cutting tool refreshes the surface at each feed step.

Starting with Albrecht's (1960) analysis of friction, Arrazola and Meslin (2002) and later Arrazola et al. (2008) proposed that the graph of feed versus cutting force has a linear trend at high feed rates, so the derivative of two force components can be used to find friction coefficients (see Eq. (1)).

$$\mu - tg\left(tg^{-1}\left(\frac{dF_f}{dF_C}\right) + \gamma_1\right) \quad (1)$$

Beginning with Zorev (1963), many researchers have considered the coefficient of friction during machining processes to be quasi-steadily distributed (quasi-steady-state assumption) along the friction distance, so they defined a mean friction coefficient along the friction face for a zero rake angle (Eq. (2)).

$$\mu = \frac{F_f}{F_C} \quad (2)$$

This coefficient changed mostly with the normal force, because the frictional force was usually constant. Rake angle, angle of inclination, and uncut chip thickness are parameters that affect the friction coefficient. Two zones of chip flow (elastic and plastic) could be defined, and during the elastic contact, the ratio between the shear stress and the normal stress along the rake face gives the mean friction coefficient. This idea was used by researchers to develop numerical models and analytical deductions. Moufki et al. (1998) proposed improvements to this method by considering the mean friction coefficient to be dependent on mean temperature.

In another approach, Albrecht (1960) believed that ploughing plays a significant yet falsely neglected role during machining processes, and accounting for this effect is necessary in order to model these processes. He believed that calculating a mean friction coefficient, and then deducting the effect of ploughing force could be a good way to approximate the solution (Eq. (3)).

$$\mu = \frac{F_f - F_{f_0}}{F_C - F_{C_0}} \quad (3)$$

Sutter and Molinari (2005) used this approach and called this the real friction coefficient, with edge forces deducted from the measured forces in tangential and normal force components, and then taking the ratio between these results. Özlü et al. (2009) and later Molinari et al. (2011) separated the friction coefficient into two components, as apparent and sliding friction coefficients. The apparent friction coefficient ($\mu_{ap}$) is considered as the ratio of total friction and normal forces on the entire rake face (Eq. (4)). The sliding friction coefficient ($\mu_{sl}$) is considered as the ratio of the friction and normal forces acting on the sliding region along the rake face (Eq. (5)).

$$\mu_{ap} = \frac{F_c tg(\gamma_1) + F_f}{f_c - F_f tg(\gamma_1)} \quad (4)$$

$$\tau = \mu_{sl}\sigma \quad (5)$$

They believed that the ratio of measured friction and normal forces is equal to sliding friction coefficient ($\mu_{sl}$), where the apparent friction coefficient ($\mu_{ap}$) is dependent on tool–chip contact length, plastic contact length, and normal stress on the rake face.

When there is no sticking in the friction zone, the sliding, apparent and mean friction coefficients would be equivalent to each other. This friction definition reveals more detailed friction than using a mean friction coefficient. However, experimental determination of friction coefficients by identifying plastic and elastic contact regions is quite an effort and it is not fully applicable to machining of high temperature alloys such as titanium and nickel-based alloys, where these regions are only stable during early stages of machining. In addition, creating simulation models with the Finite Element Method also becomes more complex due to additional input parameters required; therefore simpler friction models are preferred within the scope of this research.

### 1.2. Friction regions and stagnation point around tool edge

Another important issue in difficult-to-process materials is the effect of tool edge radius and the uncut chip thickness on the chip

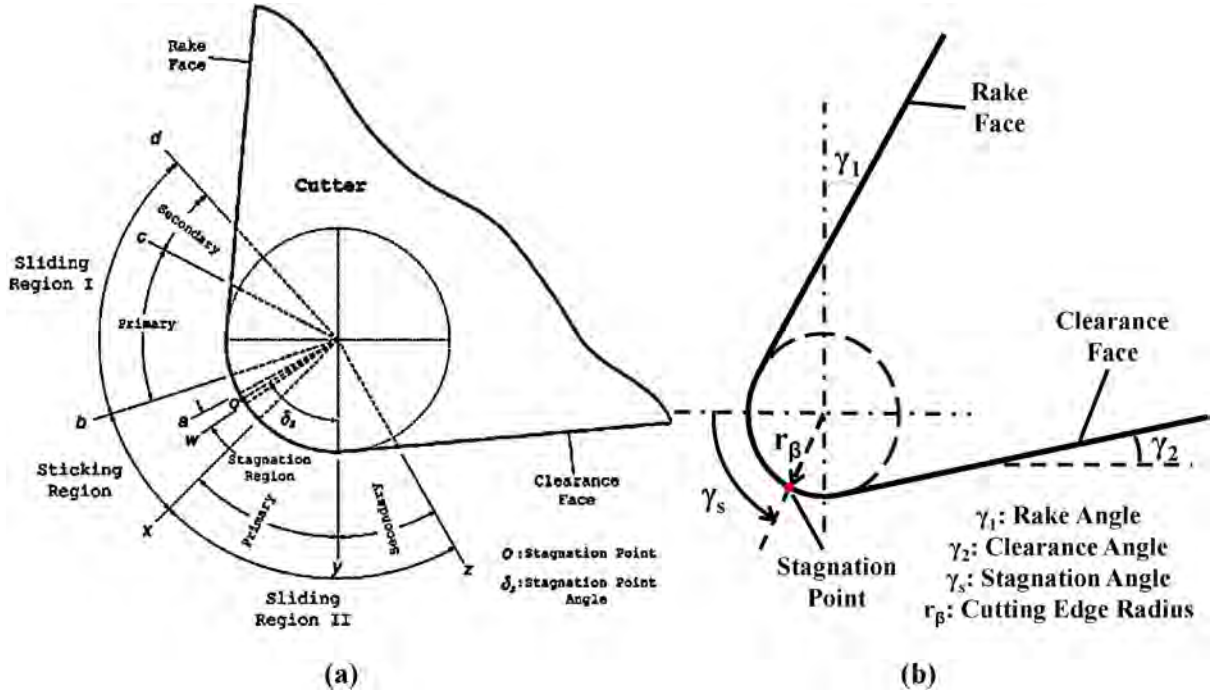


**Fig. 1.** Contact regions and stagnation point on the tool; (a) as defined by Woon et al. (2008) and (b) as defined in this study.

**Table 1**
Summary of stagnation point angle on various materials, tool geometry and cutting conditions.

| Reference | Material | $v_c$ [m/min] | $t_u$ [μm] | $r_\beta$ [μm] | $r_\beta/t_u$ [μm/μm] | $\gamma_1$ [°] | $\gamma_s$ [°] |
|---|---|---|---|---|---|---|---|
| Woon et al. (2008) | AISI 1045 | 100 | 2–20 | 10 | 0.5–5 | 10 | 31–32 |
| Kishawy et al. (2006) | AISI 4140 | 200 | 200 | 15–90 | 0.075–0.45 | 6 | 20–30 |
| Yen et al. (2004) | AISI 1020 | 130 | 200 | 50–100 | 0.25–0.5 | 12 | 25–33 |
| Fang and Xiong (2008) | Al 2024-T351 | 200–500 | 49–122 | 58 | 0.48–1.18 | 5 | 60–70 |

formation process and its influence on wear development. During the chip formation process, the work material is separated on the surface of the tool edge into two pieces: the chip, and the machined workpiece. The separated material flows in the two direction along the tool round edge, which means that the material flow velocity is zero at one point on the tool edge, which is conventionally called the stagnation point. Woon et al. (2008) suggested sticking, sliding and stagnation contact regions around the tool edge as shown in Fig. 1a. The location of the stagnation point has been an interest to the researchers as it is considered to be important in determining the rate of tool wear, and eventually, the machined surface quality.

In such studies, researchers mostly investigated the effect of cutting edge radius, uncut chip thickness, or the ratio of these two on the location of stagnation point, or in short, stagnation angle that represents this location as summarized in Table 1. It must be noted that the conventional representation of stagnation angle is from the feed direction, whereas due to the requirements of this study, it is shown from the cutting velocity direction (Fig. 1b). This necessity results in a conversion of angles, but the results and discussions remain the same.

Fang (2003) showed that with decreasing uncut chip thickness to cutting edge radius ratio, the tool–chip contact length decreased from almost twice the uncut chip thickness to around the same value as the uncut chip thickness. Besides, Fang (2003) pointed out that with increasing stagnation angle, the effect of ploughing force decreased, as well as the average shear strain, whereas the average shear strain rate first decreased then increased. Yen et al.'s (2004) finite element analysis of orthogonal machining showed for round edge uncoated cemented carbide tools using AISI 1020 steel that the stagnation angle decreases from $\gamma_s = 33^\circ$ to 25° with the cutting edge radius increasing from $r_\beta = 50$ and 100 μm, which contradicts to most other studies (Table 1). In a similar study for AISI 4140 steel, Kishawy et al. (2006) showed that stagnation angle increases from $\gamma_s = 20^\circ$ to 30° with increasing cutting edge radius from $r_\beta = 15$ to 90 μm (Table 1). They also showed that at the stagnation point, shear stress changes sign and normal stress is close to its peak value. In a micromachining study, Woon et al. (2008) defined tool–workpiece contact friction in three regions using a Finite Element-based model, and found that the stagnation angle was around $\gamma_s = 31$–32° for $t_u = 2$–20 μm of uncut chip thickness and $v_c = 100$ m/min cutting speed, not being affected from the uncut chip thickness (Table 1). In another study, Fang and Xiong (2008) generated a new method using slip-lines to predict cutting forces and chip thickness in machining Al 2024-T351 and Copper 330. They found out that with an increase in the ratio of uncut chip thickness ($t_u$) to cutting edge radius ($r_\beta$), rake face friction coefficient does not change significantly (stays around $\mu_1 = 0.4$), while the stagnation angle increases. For the aluminum alloy Al 2024-T351, they found that the stagnation angle decreased from $\gamma_s = 67$ to 59° with uncut chip thickness increasing from $t_u = 0.049$ to 0.122 mm, whereas for the 330 Copper, the stagnation angle

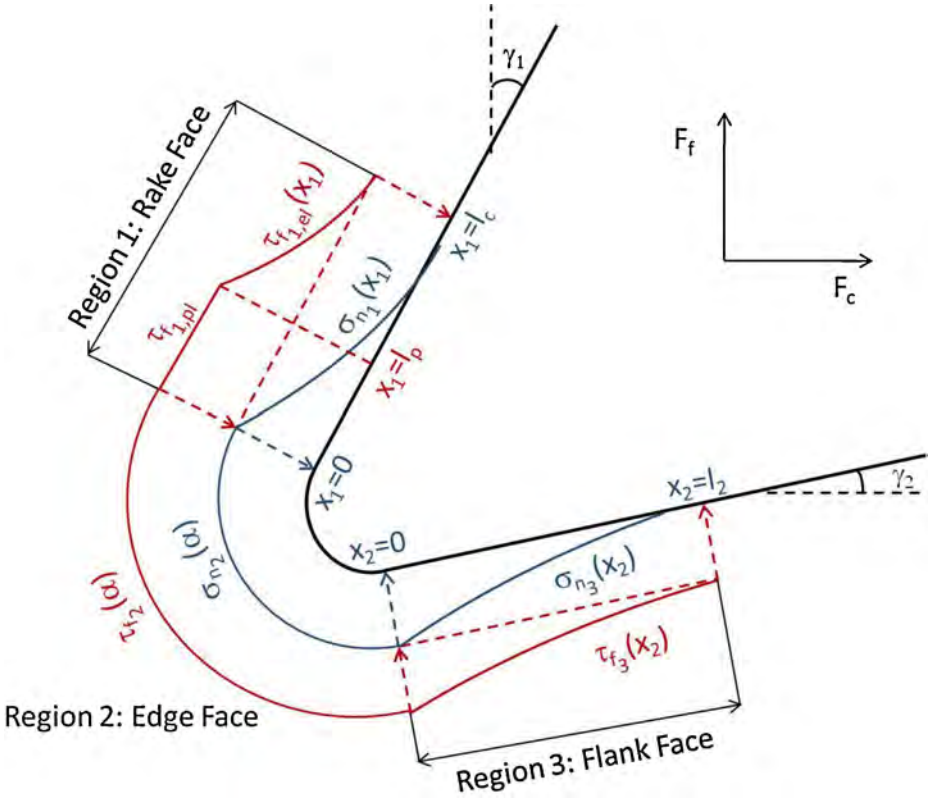


**Fig. 2.** Illustration of stress distributions on the three regions of tool.

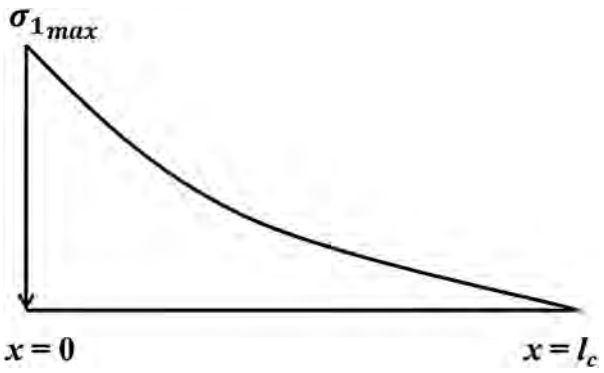


**Fig. 3.** Illustration of the normal stress along the rake face region (Region 1).

decreased from $\gamma_s = 80$ to 60° with uncut chip thickness increasing from $t_u = 0.046$ to 0.091 mm (Table 1).

## 2. Determination of friction and tool stresses for round edge cutting tool

The cutting tool, even when it is considered to be sharp, always has a rounded edge due to impossibility of infinite accuracy of the manufacturing technology of the tools. For sharp tools, this rounded edge could be assumed to have a very small radius (such as $r_\beta < 1$ μm), or a relatively small radius (such as $r_\beta = 2$–3 μm) depending on the accuracy of the tool manufacturer. With this in mind, one can assume safely that the cutting tool is always rounded at the edge, and then start the following analysis. In this analysis, the tool–workpiece/chip interface was divided into three regions (Fig. 2), and the tool is assumed to be at or close to its fresh state of geometry. Dry cutting conditions without use of coolant have been considered to eliminate additional complexity. However, method presented in this paper can be extended for coolant use.

In the first region (Region 1), the tool and the workpiece were considered to have full contact on the edge face, where the workpiece faces shearing. In this region, from the rake end of the circular region ($x_1 = 0$) to the end of the tool/chip contact ($x_1 = l_c$), tool and workpiece were assumed to have sticking and sliding friction conditions. In the third region (Region 3), from the flank end of the circular region ($x_2 = 0$) to the end of the wear length ($x_2 = l_2$), the tool is assumed to have only sliding friction conditions.

Non-linear stress distributions along the rake and flank faces of the tool and linear stress distributions along the round edge of the tool have been assumed as shown in Fig. 2. Similar stress distributions have been proposed by many researchers as reported in literature. In this assumption, normal and shear stresses shall be linearly distributed around the tool edge radius in Region 2. One end of this region is the beginning of rake face (Region 1) where is the normal stress and is the shear stress (see Figs. 3 and 4) and the other end is the beginning of the flank face (Region 3) where the normal stress becomes and shear stress becomes (see Figs. 5–7). Therefore, the contact pressure in the direction normal to the tool surfaces and frictional shear stress must be linearly distributed along Region 2 between these two end conditions for continuity once an undeformed chip thickness equal or greater than the edge radius is taken and the cutting process reaches to a steady state.

The parameters of the stress distributions on the rake fake, along the round edge and on the flank face in addition to the sliding friction coefficients at the rake and flank faces are calculated using the procedure described below, and these friction coefficients have been inserted into the FEM model created for tool stress distribution-based validations.

To start the procedure, initially five unknown variables are searched within acceptable intervals: rake ($\mu_1$) and flank ($\mu_2$) face

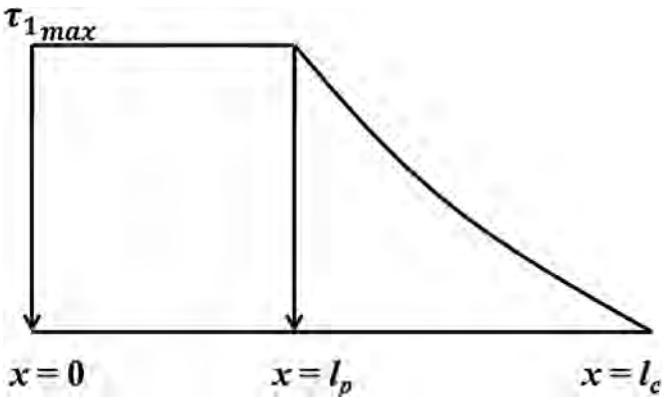


**Fig. 4.** Illustration of the frictional shear stress along the rake face region (Region 1).

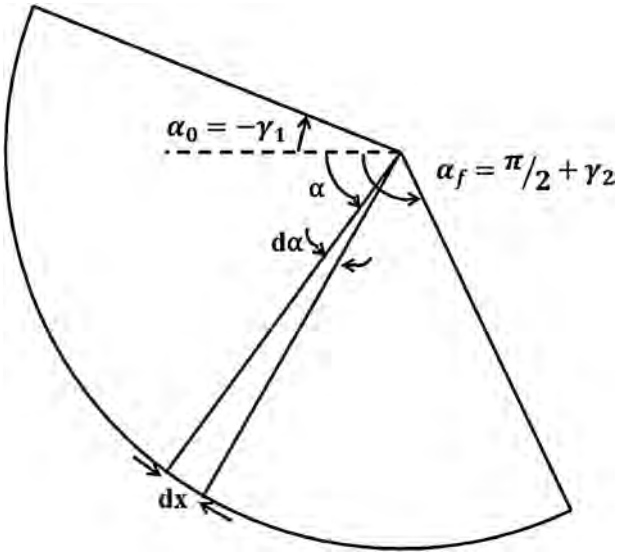


**Fig. 5.** Edge face illustration (Region 2).

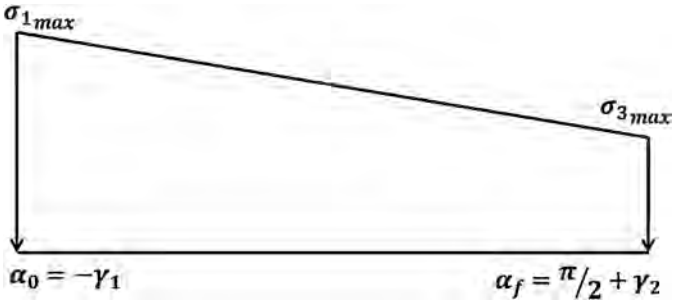


**Fig. 6.** Normal stresses on the edge face (Region 2).

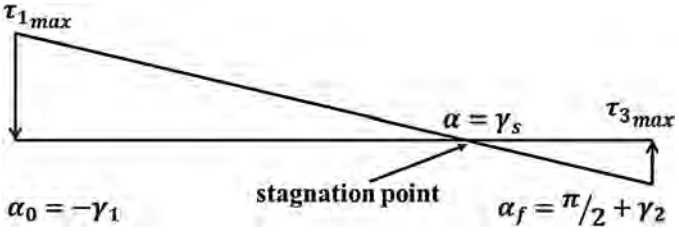


**Fig. 7.** Shear stresses on the edge face (Region 2).

friction respectively ($0 < \mu_1$ and $\mu_2 < 1$), tool–chip contact length on the rake region ($l_p \le l_c \le l_{p\_max}$), maximum normal stress on the rake region (), and the maximum normal stress on the flank region (). The normal and tangential components of forces in all three regions are calculated and converted to cutting and feed force components ($F_c$ and $F_f$, respectively), which are then summed up to result in the total cutting and feed forces:

$$F_c = F_{n_{1c}} + F_{t_{1c}} + F_{n_{2c}} + F_{t_{2c}} + F_{n_{3c}} + F_{t_{3c}} \tag{6}$$

$$F_f = F_{n_{1f}} + F_{t_{1f}} + F_{n_{2f}} + F_{t_{2f}} + F_{n_{3f}} + F_{t_{3f}} \tag{7}$$

In the first region, normal stress is assumed to have a polynomial distribution (Fig. 3):

$$\sigma_1(x_1) = \sigma_{1_{max}} \left(1 - \frac{x_1}{l_c}\right)^n \tag{8}$$

When integrated from $x_1 = 0$ to $x_1 = l_c$, normal component of the force in this region is found to be:

$$F_{n_1} = \int_0^{l_c} \sigma_{1_{max}} \left(1 - \frac{x_1}{l_c}\right)^n dx_1 = \sigma_{1_{max}} \left(\frac{l_c}{n+1}\right) \tag{9}$$

There are two different types of friction in this region (Fig. 4). The sticking friction brings plastic shear conditions, and after a certain amount of plastic contact, the chip starts to slide on the tool, which brings elastic shear conditions. Here, the shear stress on the rake face can be found as:

$$\tau_1(x_1) = \begin{cases} \tau_{1_{max}}, & 0 \le x_1 \le l_p \\ \mu_1 \sigma_1(x_1), & x_1 > l_p \end{cases} \tag{10}$$

where $\tau_{1_{max}}\ dx_1 + \mu_1 \sigma_{1_{max}} \left(1 - \frac{l_p}{l_c}\right)^n$. Then, after integrating the shear stresses from $x_1 = 0$ to $x_1 = l_c$, the total tangential force in this region can be found as shown in Eq. (11). Using the forces in the tangential and normal directions to the rake face, feed and cutting direction components (of Eqs. (6) and (7)) can be calculated using the rake angle ($\gamma_1$) (Eqs. (12)–(15)).

$$\begin{aligned} F_{t_1} &= \int_0^{l_p} \tau_{1_{max}}\, dx_1 + \int_{l_p}^{l_c} \mu_1 \sigma_{1_{max}} \left(1 - \frac{x_1}{l_c}\right)^n dx_1 \\ &= \int_0^{l_p} \tau_{1_{max}} l_p + \mu_1 \sigma_{1_{max}} \frac{l_c}{n+1} \left(1 - \frac{l_p}{l_c}\right)^{n+1} \end{aligned} \tag{11}$$

$$F_{n_{1c}} = -F_{n_1} \cos\gamma_1 = \sigma_{1_{max}} \cos\gamma_1 \left(\frac{l_c}{n+1}\right) \tag{12}$$

$$F_{n_{1f}} = -F_{n_1} \sin\gamma_1 = -\sigma_{1_{max}} \sin\gamma_1 \left(\frac{l_c}{n+1}\right) \tag{13}$$

$$F_{t_{1c}} = F_{t_1} \sin\gamma_1 = \mu_1 \sigma_{1_{max}} \sin\gamma_1 \left(\frac{nl_p + l_c}{n+1}\right) \left(1 - \frac{l_p}{l_c}\right)^n \tag{14}$$

$$F_{t_{1f}} = F_{t_1} \cos\gamma_1 = \mu_1 \sigma_{1_{max}} \cos\gamma_1 \left(\frac{nl_p + l_c}{n+1}\right) \left(1 - \frac{l_p}{l_c}\right)^n \tag{15}$$

The second contact region will be the edge face, which is the curvilinear section that is located in between the linear rake region and the linear tool wear region (Fig. 5). In this region, normal and shear stresses are assumed to be linearly changing throughout the angular profile. The normal stress is assumed to start from $\sigma_{1_{max}}$ at $\alpha = -\gamma_1$, and decrease linearly to $\sigma_{3_{max}}$ at $\alpha = \pi/2 + \gamma_2$ (Fig. 6). Hence, the normal stress distribution in the second region can be written as Eq. (16). The shear stress, on the other hand, is assumed to start from $\sigma_{1_{max}}$ at $\alpha = -\gamma_1$, and decrease linearly to $\sigma_{3_{max}}$ at $\alpha = \pi/2 + \gamma_2$ (Fig. 7). Due to the directions of the flow of the chip and the machined workpiece, the direction of the maximum shear stress at the flank face ($\sigma_{3_{max}}$) is opposite to the direction of the rake face shear stress ($\sigma_{3_{max}}$), causing a stagnation point at the edge face (Kishawy et al., 2006), and the stagnation angle can be found by Eq. (17). As a result of the assumptions, the shear stress distribution in the second region can be written as Eq. (18). Integrating these functions through the whole region, one can find the force components in cutting and feed directions (Eqs. (19)–(22)).

$$\sigma_2(\alpha) = \frac{(\sigma_{3_{max}} - \sigma_{1_{max}})\alpha + (\gamma_1 \sigma_{3_{max}} + (\pi/2 + \gamma_2)\sigma_{1_{max}})}{\pi/2 + \gamma_1 + \gamma_2} \tag{16}$$

$$\gamma_s = \frac{(\pi/2 + \gamma_2)\tau_{1_{max}} - \gamma_1 \tau_{3_{max}}}{\tau_{1_{max}} + \tau_{3_{max}}} \tag{17}$$

$$\tau_2(\alpha) = -\frac{(\tau_{3_{max}} + \tau_{1_{max}}\alpha + (\gamma_1 \tau_{3_{max}} - (\pi/2 + \gamma_2)\tau_{1_{max}}))}{\pi/2 + \gamma_1 + \gamma_2} \tag{18}$$

$$\begin{aligned} F_{n_{2c}} &= \int_{\alpha=-\gamma_1}^{\pi/2+\gamma_2} \sigma_2(\alpha) \cos\alpha r_\beta\, d\alpha \\ &= r_\beta \left[\sigma_{3_{max}} \sin\left(\frac{\pi}{2} + \gamma_2\right) + \sigma_{1_{max}} \sin\gamma_1 + \frac{\sigma_{1_{max}} - \sigma_{3_{max}}}{\gamma_1 + (\pi/2 + \gamma_2)} \left(\cos\gamma_1 - \cos\left(\frac{\pi}{2} + \gamma_2\right)\right)\right] \end{aligned} \tag{19}$$

$$\begin{aligned} F_{n_{2f}} &= \int_{\alpha=-\gamma_1}^{\pi/2+\gamma_2} \sigma_2(\alpha) \sin\alpha r_\beta\, d\alpha \\ &= r_\beta \left[\sigma_{1_{max}} \cos\gamma_1 - \sigma_{3_{max}} \cos\left(\frac{\pi}{2} + \gamma_2\right) - \frac{\sigma_{1\,max} - \sigma_{3\,max}}{\gamma_1 + (\pi/2 + \gamma_2)} \left(\sin\gamma_1 + \sin\left(\frac{\pi}{2} + \gamma_2\right)\right)\right] \end{aligned} \tag{20}$$

$$\begin{aligned} F_{t_{2c}} &= \int_{\alpha=-\gamma_1}^{\pi/2+\gamma_2} -\tau_2(\alpha) \sin\alpha r_\beta\, d\alpha \\ &= r_\beta \left[\sigma_{3_{max}} \cos\left(\frac{\pi}{2} + \gamma_2\right) - \tau_{1_{max}} \cos\gamma_1 + \frac{\sigma_{1_{max}} - \sigma_{3_{max}}}{\gamma_1 + (\pi/2 + \gamma_2)} \left(\sin\gamma_1 + \sin\left(\frac{\pi}{2} + \gamma_2\right)\right)\right] \end{aligned} \tag{21}$$

$$\begin{aligned} F_{t_{2f}} &= \int_{\alpha=-\gamma_1}^{\pi/2+\gamma_2} \tau_2(\alpha) \cos\alpha r_\beta\, d\alpha \\ &= r_\beta \left[\tau_{3_{max}} \sin\left(\frac{\pi}{2} + \gamma_2\right) + \tau_{1_{max}} \sin\gamma_1 + \frac{\tau_{1_{max}} - \tau_{3_{max}}}{\gamma_1 + (\pi/2 + \gamma_2)} \left(\cos\gamma_1 - \cos\left(\frac{\pi}{2} + \gamma_2\right)\right)\right] \end{aligned} \tag{22}$$

Forces in the third region can be found similarly to the first region; except here, there is no sticking condition is assumed. Thus, normal and shear stresses, and forces in those directions can be found as shown in Eqs. ((23)–(26)). Using these forces, and the clearance angle at the flank face ($\gamma_1$), the forces in the cutting and feed force directions can also be found as in Eq. ((27)–(30)).

$$\sigma_3(x_2) = \sigma_{3_{max}} \left(1 - \frac{x_2}{VB}\right)^m \tag{23}$$

$$F_{ns} = \int_0^{VB} \sigma_{3_{max}} \left(1 - \frac{x_2}{VB}\right)^m dx_2 = \sigma_{3_{max}} \left(\frac{VB}{m+1}\right) \tag{24}$$

$$\tau_3(x_2) = \mu_2 \sigma_3(x_2) \tag{25}$$

$$F_{t_s} = \int_0^{VB} \mu_2 \sigma_{3_{max}} \left(1 - \frac{x_2}{VB}\right)^m dx_2 = \mu_2 \sigma_{3_{max}} \frac{VB}{m+1} \tag{26}$$

$$F_{n_{sc}} = F_{n_s} \cos\gamma_2 = \sigma_{3_{max}} \cos\gamma_2 \left(\frac{VB}{m+1}\right) \tag{27}$$

$$F_{n_{3f}} = -F_{n_s} \sin\gamma_2 = -\sigma_{3_{max}} \sin\gamma_2 \left(\frac{VB}{m+1}\right) \tag{28}$$

$$F_{t_{sc}} = F_{t_s} \sin\gamma_2 = \mu_2 \sigma_{3_{max}} \sin\gamma_2 \left(\frac{VB}{m+1}\right) \tag{29}$$

$$F_{t_{sf}} = F_{t_s} \cos\gamma_2 = \mu_2 \sigma_{3_{max}} \cos\gamma_2 \left(\frac{VB}{m+1}\right) \tag{30}$$

## 3. Determination of friction and tool stresses for round edge cutting tool in presence of tool flank wear

In machining operations such as milling and turning, the tool contacts the workpiece at the cutting edge, where the chip forms, and it contacts the chip at the rake face until the chip separates from the tool. Considering the previous argument about even the sharp tools being rounded with small edge radius, initially the tool contact at the flank face will not be a major contributor to the process. However, when the tool begins to wear, it is believed that the tool is rapidly worn parallel to the cutting speed direction, and orthogonal to the feed direction. Hence, when the tool becomes even slightly worn, there will be another contact region at the flank face due to tool wear. This is a common case for machining difficult-to-cut materials such as hardened steel, titanium and nickel-based alloys. As a result, contact between workpiece/chip and the tool can be divided into three basic regions in presence of flank wear (Fig. 8).

The first and third regions of this tool geometry will have similar stress and force considerations with the previous model. For the first region, there is no change at all. For the third region, the stress distributions will not change, but the conversion angle is now zero, because the wear is along the cutting direction, so the force components will be as Eqs. ((31)–(33)).

$$F_{n_{sc}} = F_{t_{sf}} = 0 \tag{31}$$

$$F_{n_{sf}} = F_{n_s} = \sigma_{3_{max}} \left(\frac{VB}{m+1}\right) \tag{32}$$

$$F_{t_{sc}} = F_{t_s} = \mu_2 \sigma_{3_{max}} \left(\frac{VB}{m+1}\right) \tag{33}$$

The second contact region will change slightly from the previous (no flank geometry change) model. As shown in Fig. 9, the angle $\alpha$ will still be equal to the rake angle of the tool at the rake face end, but at the flank face end, the cut-off angle ($\theta$) will not be equal to

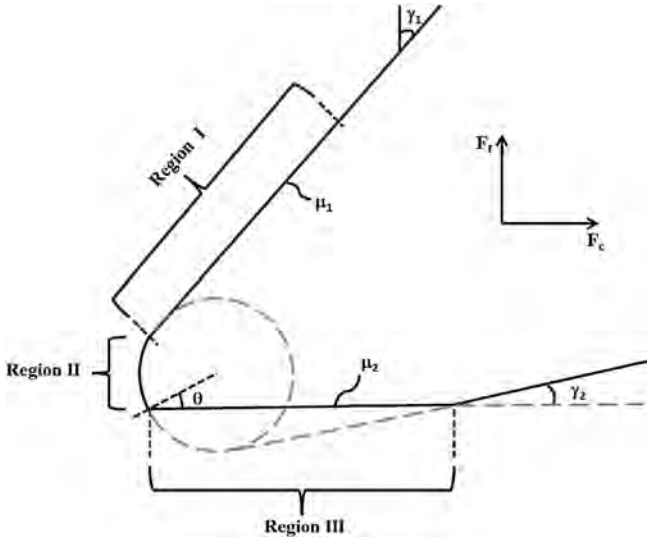


**Fig. 8.** Illustration of the three regions of cutting edge of a tool in the presence of flank wear.

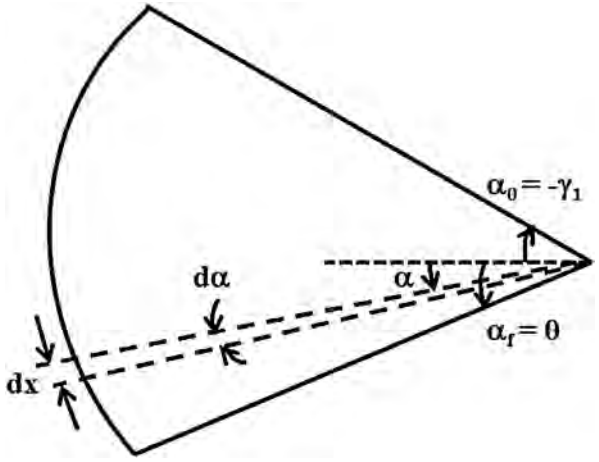


**Fig. 9.** Illustration of the tool edge face and angles (Region I).

$\pi/2 + \gamma_2$ anymore. Instead, it will be calculated using the clearance angle ($\gamma_2$), cutting edge radius ($r_\beta$), and the tool wear amount ($VB$) via Eq. (34). As with the previous model, changing from Cartesian to polar coordinates helps in analyzing this region, so the stresses can be shown as a function of $\alpha$. The linear changing assumption of normal and shear stresses is still used, and it will be as shown in Figs. 10 and 11. Note that the angle at the flank face is shown as $\theta$ rather than the angle used in the previous model ($\pi/2 + \gamma_2$), and the normal and shear stresses at this point are shown differently ($\tilde{\sigma}_2$ and $\tilde{\tau}_2$ rather than $\sigma_{3_{max}}$ and $\tau_{3_{max}}$). The stagnation angle can be calculated similarly to the previous model; only the values will be different (Eq. (35)).

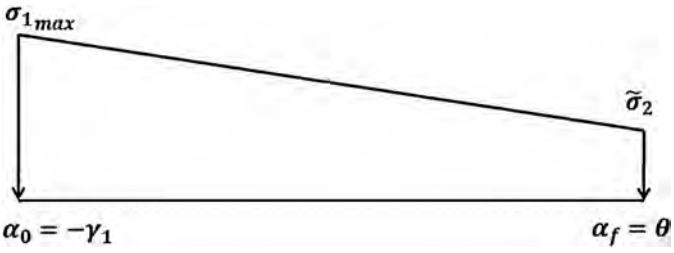


**Fig. 10.** Illustration of the normal stress along the edge face region (Region II).

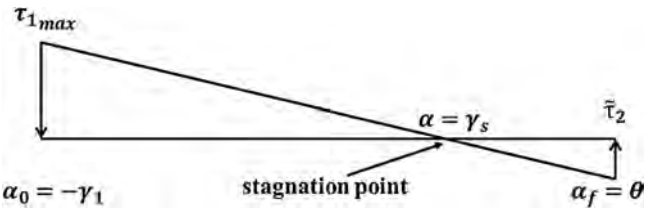


**Fig. 11.** Illustration of the frictional shear stress along the edge face region (Region II).

Analyzing the tool geometry (Fig. 8), one would realize that there is continuity in geometry from the rake face (Region I) to the edge face (Region II), so the stresses should be continuous as well, similar to the previous model. However, the geometry is not continuous at the beginning of the flank face, due to tool wear, which is the reason for the different values of normal and shear stress shown in Figs. 10 and 11. Here, the vector sum of the shear and normal stresses at the flank face end should be equal to the vector sum of the shear and normal stresses at the beginning of the flank face (Eq. (36)). Using this equation, the unknown normal and shear stresses at the flank face end of Region II can be found as shown in Eqs. ((37) and (38)). Then, the functions of normal and shear stress with changing angle ($\alpha$) in this region will become as Eqs. ((39) and (40)). Taking the integral through the whole region, the tangential and normal components of force acting on the cutting and feed directions can be found (Eq. (39) and (40)).

$$\theta = \gamma_2 + \sin^{-1}\left(1 - \frac{VB\sin\gamma_2}{r_\beta}\right) \tag{34}$$

$$\gamma_s = \frac{\theta\tau f_{1\max} - \gamma_1\tilde{\tau}_2}{\tau f_{1\max} - \tilde{\tau}_2} \tag{35}$$

$$\vec{\tilde{\sigma}_2} + \vec{\tilde{\tau}_2} = \overrightarrow{\alpha_{3\max}} + \overrightarrow{\tau_{3\max}} \tag{36}$$

$$\tilde{\sigma}_2 = \sigma_{3\max}(\mu_2\sin\theta - \cos\theta) \tag{37}$$

$$\tilde{\tau}_2 = \sigma_{3\max}(\mu_2\cos\theta - \sin\theta) \tag{38}$$

$$\sigma_2(\alpha) = \left(\frac{\tilde{\sigma}_2 - \sigma_{1\max}}{\gamma_1 + \theta}\right)(\alpha + \gamma_1) + \sigma_{1\max} \tag{39}$$

$$\tau_2(\alpha) = \left(\frac{\tilde{\tau}_2 - \tau_{1\max}}{\gamma_1 + \theta}\right)(\alpha + \gamma_1) + \tau_{1\max} \tag{40}$$

$$\begin{aligned} F_{n_{2c}} &= \int_{\alpha=-\gamma_1}^{\theta} \sigma_2(\alpha)\cos\alpha r_\beta\,d\alpha \\ &= r_\beta\left[\tilde{\sigma}_2\sin\theta + \sigma_{1\max}\sin\gamma_1 + \frac{\sigma_{1\max} - \tilde{\sigma}_2}{\gamma_1 + \theta}(\cos\gamma_1 - \cos\theta)\right] \end{aligned} \tag{41}$$

$$\begin{aligned} F_{n_{2f}} &= \int_{\alpha=-\gamma_1}^{\theta} \sigma_2(\alpha)\sin\alpha r_\beta\,d\alpha \\ &= r_\beta\left[\sigma_{1\,\max}\cos\gamma_1 - \tilde{\sigma}_2\cos\theta - \frac{\sigma_{1\,\max} - \tilde{\sigma}_2}{\gamma_1 + \theta}(\sin\gamma_1 - \sin\theta)\right] \end{aligned} \tag{42}$$

$$\begin{aligned} F_{t_{2c}} &= \int_{\alpha=-\gamma_1}^{\theta} -\tau_2(\alpha)\sin\alpha r_\beta\,d\alpha \\ &= r_\beta\left[\tilde{\tau}_2\cos\theta - \tau_{1\max}\cos\gamma_1 + \frac{\tau_{1\max} - \tilde{\tau}_2}{\gamma_1 + \theta}(\sin\gamma_1 + \sin\theta)\right] \end{aligned} \tag{43}$$

$$\begin{aligned} F_{t_{2f}} &= \int_{\alpha=-\gamma_1}^{\theta} \tau_2(\alpha)\cos\alpha r_\beta\,d\alpha \\ &= r_\beta\left[\tilde{\tau}_2\sin\theta - \tau_{1\max}\sin\gamma_1 + \frac{\tau_{1\max} - \tilde{\tau}_2}{\gamma_1 + \theta}(\cos\gamma_1 - \cos\theta)\right] \end{aligned} \tag{44}$$

There is a limitation to the set of parameters in this study; that is, the selection of tool flank wear should be done according to the constraints given in Eq. (45) (in order to be able to calculate $\theta$). These are basically what the geometry allows, and with less or more of a tool flank wear length ($VB$) than permitted; only the calculations will change slightly, and the theory behind this study will still be applicable. However, with a typical selection of clearance angle ($\gamma_2$) and cutting edge radius ($r_\beta$), the tool flank wear length limits are virtually between the minimum possible tool flank wear length after a very short machining operation to a maximum possible tool flank wear length after a very long machining operation (without tool chipping). Also, the friction coefficient at the flank face ($\mu_2$) should be selected according to the constraint given in Eq. (46). This is only so that the frictional shear stress at the flank face end of the edge face region ($\tilde{\tau}_2$) is calculated negative, and the stagnation point falls at the edge face. If this constraint is not satisfied, the stagnation point cannot be calculated. Hence, the formulation given here is capable of covering almost all the geometrical selections.

$$2\sin\gamma_2 < \frac{VB}{r_\beta} < 1 + \frac{1}{\sin\gamma_2} \tag{45}$$

$$\mu_2 < \frac{1}{\tan\theta} \tag{46}$$

## 4. Search and optimization algorithm for the friction determination methodology

Once all of the force components are calculated, they should be added up to find the resultant forces in the cutting and feed force directions (Eqs. (6) and (7)). These will correspond to the measurements during the orthogonal cutting tests, and they should be compared to find the right set of variables. The geometrical variables are the cutting edge radius ($r_\beta$), the rake angle ($\gamma_1$), the clearance angle ($\gamma_2$), and the tool flank wear angle ($\theta$). The first three are geometrical constraints from the tool, and the last one will be calculated. The contact variables are the total tool–chip contact length ($l_c$), the plastic tool–chip contact length ($l_p$), and the tool flank wear length ($VB$). These are not known prior to the simulations, and should be searched at the initial iteration. The polynomial variables ($m$, $n$) are also not known and should be searched at the initial iteration (or they could be assumed a value for the first iteration). The stress variables ($\sigma_{1\max}$, $\tilde{\sigma}_2$, $\sigma_{3\max}$, $\tau_{1\max}$, $\tilde{\tau}_2$, $\tau_{3\max}$) are also not known prior to the first iteration, and they should be searched at the first iteration. However, the shear and normal stresses at the rake face and flank face regions are related to each other with the coefficients of friction, and the shear and normal stresses in the edge face region at the flank face end are calculated (Eq. (37)–(38)). Hence, there are essentially only two stress variables ($\sigma_{1\max}$, $\sigma_{3\max}$) to search for in addition to friction coefficients and stress distribution exponents. These tool friction and stress distribution variables are searched at every iteration (see Fig. 12 for illustration of the methodology and its algorithm). At the initial iteration, all the unknown variables are searched within meaningful limits as indicated with constraints. They are selected at random, and for each set of selection, forces in cutting and feed directions are found. These forces are compared to the measured forces from orthogonal cutting tests, and the error between the measured and calculated forces are used in the algorithm so that a total error is assigned to each set of variables (Fig. 12).

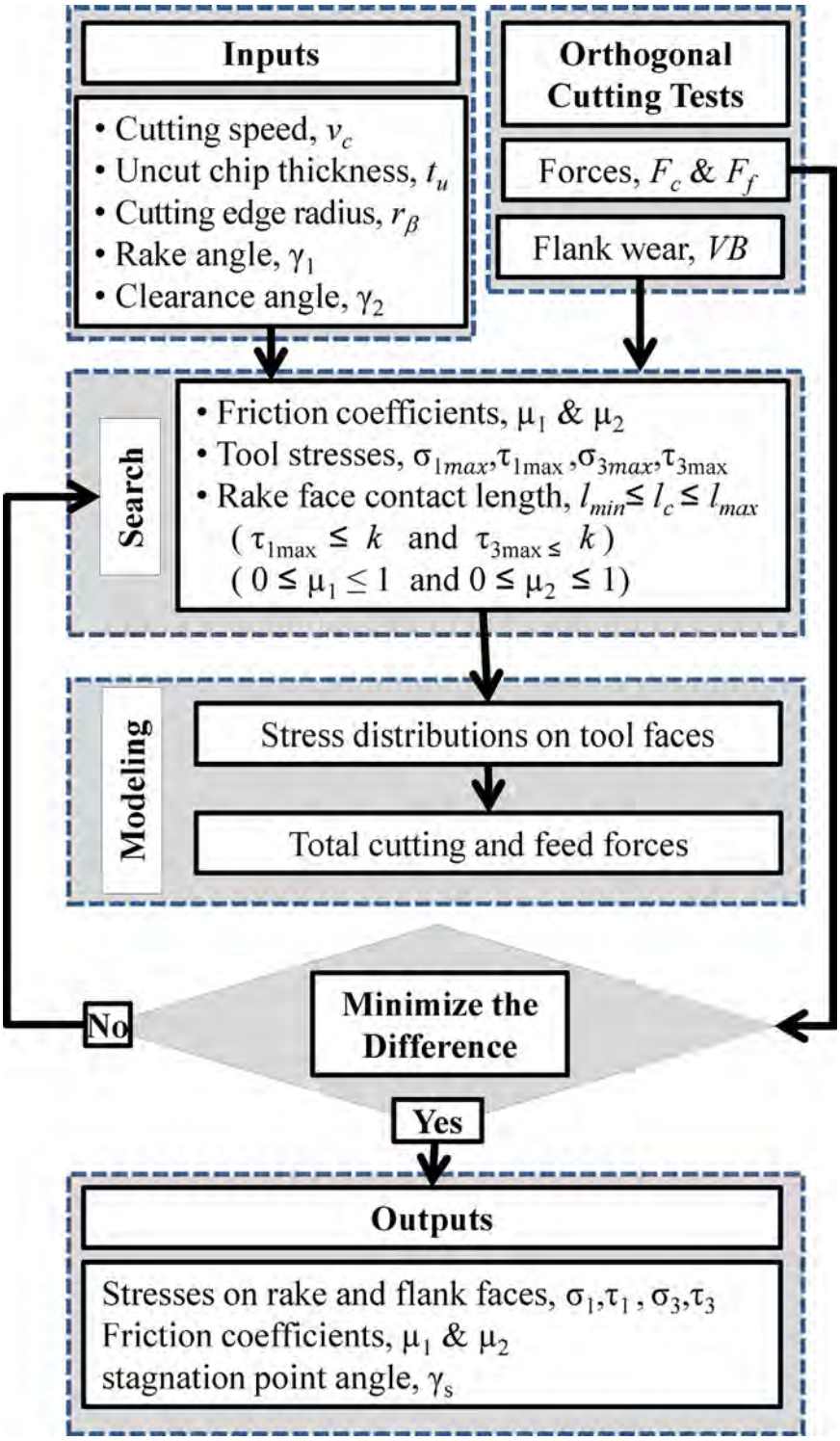


**Fig. 12.** Flow chart for friction determination methodology and its algorithm.

There exist several unknowns to be searched and identified properly in this method as very well can be noticed. These unknown values such as contact length, friction coefficients, and stress levels have been searched within a feasible range for each parameter. There are a number of constraints have been used as the ranges of possible solutions have been searched and unique solution sets have been identified with an iterative approach as outlined in the algorithm discussion of the paper. Friction coefficients determined used as input in FEM simulations and methodology has been repeated until satisfactory agreements in stress distributions have been reached.

The selection of variables is done a satisfactory amount of times, and each random set of variables has an error assigned to it. After enough number of sets are collected, the resultant variable set is

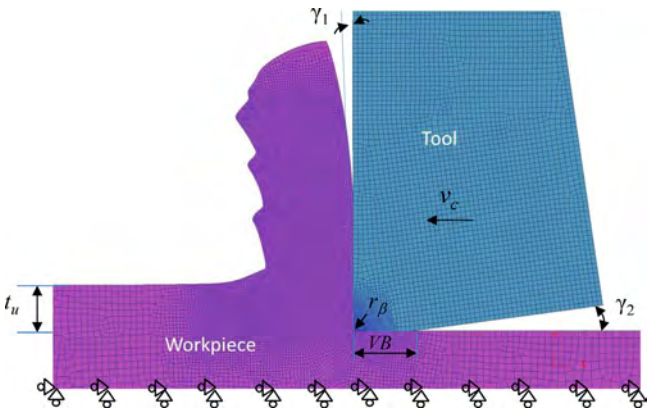


**Fig. 13.** Finite element model for orthogonal cutting.

found using Eq. (47), where $x_R$ is the resultant variable, $x_i$ is the $i$th unknown (searched) variable, $e_i$ is the error assigned to that variable, and $N$ is the total number of variables.

$$x_R = \frac{\sum_{i=1}^{N} x_i/\theta_i}{\sum_{i=1}^{N} 1/\theta_i} \tag{47}$$

After the initial calculation of the unknown variables, the resultant variable set (friction coefficients) is passed to the Finite Element-based simulations, the simulation reaches steady-state of chip formation at forces comparable to the measured forces, and the stress fields at the rake and flank faces are extracted (Fig. 11). When the stresses vs. the distances are fit to a power curve, the maximum normal ($\sigma_{1\max}$, $\sigma_{3\max}$) and frictional shear stresses ($\tau_{1\max}$, $\tau_{3\max}$) at the rake face and flank face regions as well as the polynomial coefficients ($m$, $n$) can be found. Also using the rake face stresses, one can find the total and plastic tool–chip contact lengths ($l_c$ and $l_p$), and the stagnation point can be confirmed using the shear stress vector representation. At the next iteration of the friction determination method, these values are used instead of searching for all of them. As a result, at each iteration, the friction coefficients are the only ones being searched (and then passed on to the FEM-based simulation model), and the remaining unknown parameters are retrieved from FEM-based simulations. When the friction coefficients are very close to each other within tolerable limits at two consecutive iterations, the algorithm is stopped and the friction coefficients are determined as the final values (Fig. 12).

## 5. Comparison of results and validations

For all the cutting conditions that the friction coefficient determination method was utilized, Finite Element-based simulations were also designed and conducted. Using these simulations, forces and stress fields of these machining processes were predicted and compared with the results from experiments and the friction determination method. In these Finite Element-based simulations, chip formation in orthogonal cutting was modeled by using DEFORM-2D updated Lagrangian simulation software as shown in Fig. 13. The workpiece material was assumed to be elastic-viscoplastic, so that the physics of the process would be simulated in the best way. The tool material was initially set as rigid, but after the chip formation was achieved, it was changed to elastic. This way, the stress fields on the tool can also be obtained and compared to the friction determination method results. The heat conduction coefficient ($h$) was taken as 100,000 W/m$^2$ K, so that the temperature rise in the tool can be simulated rapidly. Mechanical and thermo-physical properties of work and tool materials were defined as temperature ($T$) dependent, and are given in Table 2 for both Ti-6Al-4V and IN-100. For flow softening, a modified material model that includes the temperature-dependent flow softening effect in addition to strain and strain rate hardening and thermal softening effects is used (Eq. (48)). The parameters in this equation for both Ti-6Al-4V and IN-100 are given in Table 3. Friction between the chip and tool materials were defined as hybrid on the rake face, including shear friction and Coulomb friction, as described in the previous sections. The friction between the workpiece and tool material on the flank face was defined as only Coulomb friction, due to the nature of the friction determination method. All the simulations were run until chip formation was clearly observed, and temperatures and forces reach a steady state with the rigid tool assumption. This corresponded to 1–1.5 ms for all of the simulations. After steady-state values were achieved, simulations were run for a short while under the elastic tool assumption where the stresses on the tool can also reach steady state, which corresponded to approximately 0.1 ms for all of the simulations.

$$\sigma = [A + B\varepsilon^n]\left[1 + C\ln\frac{\dot{\varepsilon}}{\dot{\varepsilon}_0}\right]\left[1 - \left(\frac{T - T_o}{T_m - T_o}\right)^m\right] \times \left[D + (1 - D)\left[\tanh\left(\frac{1}{(s + p)^r}\right)\right]^s\right] \tag{48}$$

### 5.1. Results of the friction determination

As indicated in the flow chart in Fig. 12, proposed friction determination methodology requires orthogonal cutting test data with various tool geometry considerations such as rake angle and cutting edge radius as well as a range of cutting speed and uncut chip thickness. For this reason, orthogonal cutting tests reported in literature for Ti-6Al-4V titanium alloy and IN-100 nickel-based alloy have been utilized.

Wyen and Wegener (2010) reported experimental results of orthogonal turning tests conducted on Ti-6Al-4V using uncoated carbide tools with a rake angle of $\gamma_1 = 10^\circ$, cutting edge radii of $r_\beta = 20$ and 30 μm, cutting speeds of $v_c = 30$ and 70 m/min and uncut chip thicknesses of $t_u = 0.06$ and 0.1 mm. They also proposed a method for determining cutting edge radius and ploughing forces in their study.

Özel (2009) reported experimental results of orthogonal disk turning tests for IN-100 nickel-based alloy using uncoated carbide tools with edge radii of $r_\beta = 10$ and 25 μm and rake angles of $\gamma_1 = 0^\circ$ and $3^\circ$, cutting speed of $v_c = 12$ and 24 m/min and uncut chip thicknesses of $t_u = 0.05$ and 0.1 mm. He also reported about measured forces, chip geometry and tool edge conditions.

Friction determination method is utilized and after all the forces are calculated, they are summed up in cutting and feed directions (Eq. (6) and (7)), and compared to the test data of Wyen and Wegener (2010) for Ti-6Al-4V and the test data of Özel (2009) for IN-100. The searched variables are optimized according to the measured data, and as a result of this search, the friction coefficient values that induced the minimum difference between the measured and calculated forces were accepted as the Coulomb friction coefficients in corresponding regions. After comparing the results with the orthogonal cutting test force measurements of Wyen and Wegener (2010) for Ti-6Al-4V and of Özel (2009) for IN-100, the normalized non-linear relationships between the two friction coefficients (rake face $\mu_1$, and flank face $\mu_2$) and cutting speed ($v_c$ in m/min), uncut chip thickness ($t_u$ in mm), and cutting edge radius ($r_\beta$ in mm) were found to be as given in Eq. (49) and (50), where the coefficients (after normalizing with mean vales of cutting speed, feed rate, and cutting edge radius values from experiments) are given in Table 4 for Ti-6Al-4V and in Table 5 for IN-100. These expressions are obtained with high coefficient of determination values ($R^2 > 0.9$) indicating the goodness of the fit for using these

**Table 2**
Mechanical and thermo-physical properties of work and tool materials used in FE simulations.

| Property | WC/Co | Ti-6Al-4V | IN-100 |
|---|---|---|---|
| $E$ (T) [MPa] | $5.6 \times 10^5$ | $0.7412 \times T + 113375$ | $-61000 \times T + 278000$ |
| $\alpha_t$ (T) [mm/mm·°C] | $4.7 \times 10^{-6}$ | $3.10^{-9} \times T + 7.10^{-6}$ | $10^{-5} e^{0.0849T}$ |
| $\lambda(T)$ [W/m °C] | 55 | $7.039e^{0.0011T}$ | $10.409e^{0.0903T}$ $418.63e^{0.0433T}$ |
| $c_p(T)$ [N/mm$^2$ °C] | $0.0005 \times T + 2.07$ | $2.24e^{0.0007T}$ | |

**Table 3**
Material model parameters used in FE simulations.

| Alloy | $A$ [Mpa] | $B$ [MPa] | $n$ | $C$ | $\dot{\varepsilon}_0$ | $m$ | $D$ | $p$ | $R$ | $s$ |
|---|---|---|---|---|---|---|---|---|---|---|
| Ti-6Al-4V | 1000 | 625 | 0.55 | 0.029 | $10^{-5}$ | 0.995 | 0.48 | 0 | 1.2 | 2.7 |
| IN-100 | 1350 | 1750 | 0.65 | 0.017 | $10^{-3}$ | 1.3 | 0.6 | 0 | 1.0 | 5.0 |

**Table 4**
Coefficients of the non-linear relationships for rake and flank face friction coefficients for Ti-6Al-4V ($R^2$ values for $\mu_1$ and $\mu_2$ are 0.972 and 0.928 respectively).

| | $a$ | $b$ | $c$ | $d$ | $e$ | $f$ | $G$ | $h$ |
|---|---|---|---|---|---|---|---|---|
| $\mu_1$ | −0.08 | −0.12 | 0.5 | 0.01 | 0.02 | −0.03 | 0.01 | 0.66 |
| $\mu_2$ | 0.04 | 0.12 | −0.17 | −0.03 | −0.03 | 0.08 | −0.02 | 1 |

**Table 5**
Coefficients of the non-linear relationships for rake and flank face friction coefficients for IN-100 ($R^2$ values for $\mu_1$ and $\mu_2$ are 0.959 and 0.943 respectively).

| | $a$ | $b$ | $c$ | $d$ | $e$ | $f$ | $g$ | $h$ |
|---|---|---|---|---|---|---|---|---|
| $\mu_1$ | −0.06 | −0.13 | 0.58 | −0.04 | −0.01 | −0.06 | 0.01 | 0.72 |
| $\mu_2$ | 0.05 | 0.15 | −0.24 | −0.13 | 0.05 | 0.06 | 0.04 | 0.98 |

models for future predictions. As also depicted by the coefficients of the equations, it was found that rake face friction coefficient ($\mu_1$) decreases when the feed rate is increased, increases significantly when the cutting edge radius is increased, and decreases slightly when the cutting speed is increased, with the non-linear terms being insignificant compared to the linear terms. On the other hand, the flank face friction coefficient ($\mu_2$) increases slightly with increasing uncut chip thickness (or feed rate), does not change significantly with the cutting speed, and decreases significantly with increasing cutting edge radius at lower feed rates (0.05–0.06 mm) but decreases only slightly with increasing cutting edge radius at higher feed rates (0.1–0.2 mm). This is reflected on the non-linear term that includes uncut chip thickness and cutting edge radius ($f_2$) being considerably higher than the other coefficients when normalized.

$$\mu_1 = a_1 v_c + b_1 t_u + c_1 r_\beta + d_1 v_c t_u + e_1 v_c r_\beta + f_1 t_u r_\beta + g_1 v_c t_u r_\beta + h_1 \quad (49)$$

$$\mu_2 = a_2 v_c + b_2 t_u + c_2 r_\beta + d_2 v_c t_u + e_1 v_c r_\beta + f_2 t_u r_\beta + g_2 v_c t_u r_\beta + h_2 \quad (50)$$

The semi-empirical friction expressions that are given in Eq. (49) and (50) can be assumed to represent the cutting condition intervals where $v_c$ = 10–110 m/min, $t_u$ = 0.06–0.2 mm, $r_\beta$ = 10–50 μm for Ti-6Al-4V, and $v_c$ = 12–24 m/min, $t_u$ = 0.05–0.1 mm, $r_\beta$ = 10–25 μm for IN-100, since the measured data used covers these intervals. It should be noted that the values of cutting speed, feed, and cutting edge radius are normalized by using their average values, e.g. cutting speed used in the equations would not be $v_c$ = 100 m/min, but $v_c = 100/v_{c\_ave}$, where $v_{c\_ave}$ is the average cutting speed from all the experiments.

### 5.2. Validation on nickel-based alloy (IN-100) machining data

Stress distribution based validation studies have been conducted to compare tool stresses calculated from friction determination method and stress distribution outputs obtained from FE-based simulations when friction coefficients are utilized in hybrid friction model as input. FE-based simulation results for the nickel-based alloy IN-100 can be found in Table 6. The simulations were run for two different rake angles ($\gamma_1$ = 0° and 3°), two different edge radii ($r_\beta$ = 10 and 25 μm), two different cutting speed ($v_c$ = 12 and 24 m/min), and two different uncut chip thickness ($t_u$ = 0.05 and 0.1 mm), a total of 16 cutting conditions. Experimental results reported in (Özel, 2009) were gathered for all the conditions, as the cutting and tangential forces are used within the algorithm. The results presented in this table represent the last iteration, and the reason to terminate the iterations was that in the previous iteration, change in friction coefficients on the rake and flank faces ($\mu_1$ and $\mu_2$) were less than 1% (Table 6). As a result, it is safe to say that in all cutting conditions, friction coefficient on the rake face between tool and the chip was around $\mu_1$ = 0.7, while the friction coefficient on the flank face between tool and worn workpiece was found to be around $\mu_2$ = 0.62. FE-based simulations for the same 16 conditions were run with DEFORM-2D FE-based simulation software. At each iteration, stress fields were extracted from the simulations, and Fig. 14b shows a representative stress field as simulation output. These stress fields were fit into an exponential curve, and Fig. 14a shows a sample comparison of stress fields extracted from the simulations and the stress fields obtained from the friction determination method. These are the results of the last iteration, so the stress field has not changed much between two consecutive iterations.

The influence of tool rake angle, geometry and cutting conditions has been investigated by utilizing stresses extracted from friction determination method and FE-based simulations. These

**Table 6**
Search algorithm results compared to orthogonal cutting results for IN-100.

| Experimental | | | | | | FEM Results | | | | | | | FDM Results | | | | | | |
|---|---|---|---|---|---|---|---|---|---|---|---|---|---|---|---|---|---|---|---|
| $r_\beta$ [μm] | $v_c$ [m/min] | $t_u$ [mm] | $b$ [mm] | $F_t$ [N] | $F_c$ [N] | $\sigma_{1max}$ [MPa] | $n$ | $\sigma_{3max}$ [MPa] | $m$ | $l_c/t_u$ | $l_p/t_u$ | $F_t$ [N] | $F_c$ [N] | $\mu_1$ | $\mu_2$ | $\tau_{1max}$ [MPa] | $\bar{\sigma}_2$ [MPa] | $\bar{\tau}_2$ [MPa] | $\gamma_s$ [°] |
| $\gamma_1 = 0°$ | | | | | | | | | | | | | | | | | | | |
| 10 | 12 | 0.05 | 3.52 | 1185 | 1470 | 3712 | 0.50 | 318 | 0.51 | 3.07 | 0.55 | 887 | 1447 | 0.70 | 0.62 | 2346 | 285 | −244 | 15.9 |
| 10 | 12 | 0.1 | 3.52 | 1949 | 2166 | 3389 | 0.51 | 607 | 0.50 | 2.39 | 0.64 | 1419 | 2591 | 0.70 | 0.62 | 1987 | 543 | −465 | 14.2 |
| 10 | 24 | 0.05 | 2.99 | 1090 | 1013 | 3900 | 0.52 | 706 | 0.52 | 2.66 | 0.58 | 801 | 1214 | 0.70 | 0.62 | 2396 | 631 | −541 | 14.3 |
| 10 | 24 | 0.1 | 2.99 | 1692 | 1602 | 4281 | 0.52 | 1463 | 0.47 | 2.08 | 0.54 | 1307 | 2117 | 0.70 | 0.62 | 2558 | 1306 | −1122 | 12.2 |
| 25 | 12 | 0.05 | 3.09 | 1074 | 967 | 3180 | 0.48 | 1120 | 0.51 | 2.67 | 0.31 | 939 | 1221 | 0.70 | 0.62 | 2092 | 1304 | −193 | 45.6 |
| 25 | 12 | 0.1 | 3.09 | 1756 | 1854 | 3359 | 0.49 | 2158 | 0.50 | 2.32 | 0.28 | 1505 | 2024 | 0.70 | 0.62 | 2207 | 2508 | −377 | 42.5 |
| 25 | 24 | 0.05 | 2.45 | 882 | 707 | 3155 | 0.47 | 1672 | 0.50 | 2.47 | 0.30 | 720 | 904 | 0.70 | 0.62 | 2080 | 1941 | −295 | 43.6 |
| 25 | 24 | 0.1 | 2.45 | 1415 | 1513 | 3723 | 0.47 | 1790 | 0.54 | 2.12 | 0.40 | 1105 | 1615 | 0.70 | 0.62 | 2359 | 2081 | −311 | 44.0 |
| $\gamma_1 = 3°$ | | | | | | | | | | | | | | | | | | | |
| 10 | 12 | 0.05 | 2.45 | 768 | 885 | 3443 | 0.53 | 636 | 0.50 | 2.74 | 0.49 | 561 | 980 | 0.70 | 0.62 | 2165 | 569 | −488 | 13.7 |
| 10 | 12 | 0.1 | 2.45 | 1292 | 1645 | 3961 | 0.50 | 797 | 0.49 | 2.07 | 0.57 | 848 | 1693 | 0.70 | 0.62 | 2355 | 713 | −611 | 13.3 |
| 10 | 24 | 0.05 | 2.45 | 810 | 932 | 3869 | 0.50 | 699 | 0.51 | 2.15 | 0.59 | 617 | 941 | 0.70 | 0.62 | 2302 | 624 | −536 | 13.6 |
| 10 | 24 | 0.1 | 2.45 | 1298 | 1631 | 3419 | 0.50 | 1577 | 0.52 | 2.27 | 0.45 | 1024 | 1708 | 0.70 | 0.62 | 2139 | 1408 | −1210 | 10.1 |
| 25 | 12 | 0.05 | 3.02 | 941 | 1138 | 2971 | 0.50 | 1697 | 0.49 | 2.45 | 0.30 | 891 | 1163 | 0.70 | 0.61 | 1950 | 1969 | −300 | 42.7 |
| 25 | 12 | 0.1 | 3.02 | 1710 | 2217 | 3286 | 0.49 | 1190 | 0.52 | 2.54 | 0.27 | 1302 | 2078 | 0.70 | 0.62 | 2170 | 1385 | −206 | 45.2 |
| 25 | 24 | 0.05 | 2.96 | 1094 | 1233 | 3298 | 0.50 | 2149 | 0.53 | 2.05 | 0.35 | 858 | 1113 | 0.70 | 0.61 | 2109 | 2491 | −383 | 41.7 |
| 25 | 24 | 0.1 | 2.96 | 1506 | 2255 | 3487 | 0.51 | 2709 | 0.50 | 2.02 | 0.48 | 1302 | 1894 | 0.70 | 0.62 | 2127 | 3145 | −478 | 40.1 |

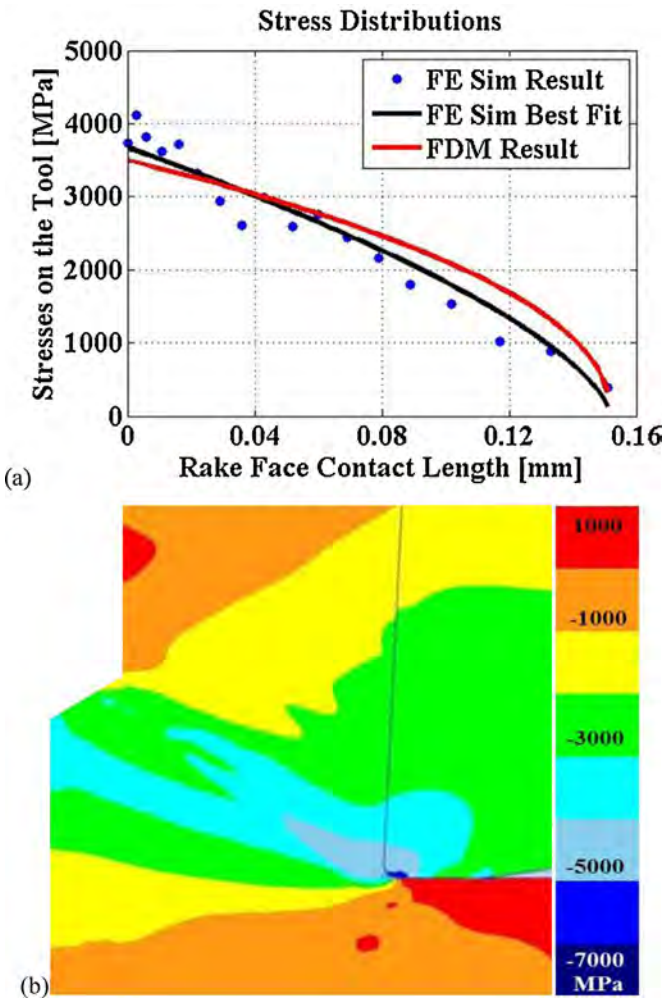


**Fig. 14.** Comparison of IN-100 (a) predicted compressive normal stresses on the tool and (b) FE-based simulation stress distribution ($v_c$ = 12 m/min, $t_u$ = 0.05 mm, $r_\beta$ = 10 μm, $\gamma_1$ = 0°).

results are presented in Figs. 15–24 where all normal stresses are compressive.

From the results, it was observed that in the cutting speed direction (hoop or tangential stress in orthogonal cutting), tensile machining-induced stresses were more apparent for lower cutting speed values ($v_c$ = 12 m/min). In this direction, stresses acting on the tool are compressive with decreasing values from the tool tip. Increasing the feed did not seem to change machining-induced stresses on the workpiece, but tool stresses became more compressive, which can change tool wear rate and consequently the surface integrity of the machined product. It was also observed that rake angle did not seem to have a significant effect on the stresses in this direction, while with increasing cutting edge radius, machining-induced stresses became less tensile. In the feed direction (longitudinal in orthogonal cutting), tensile machining-induced stresses were apparent in all conditions, increasing with cutting speed. Stresses on the tool became more compressive with increasing feed. Rake angle or edge radius did not seem to have significant effects on stress distributions in this direction. In the depth of cut direction (radial in orthogonal cutting), tensile machining-induced stresses became compressive with increasing cutting speed, while the effects of feed, rake angle, and edge radius seemed to be insignificant.

In addition, for all the simulations, the maximum shear stress on the rake face was around $\tau_{1max}$ = 2000–2500 MPa for all

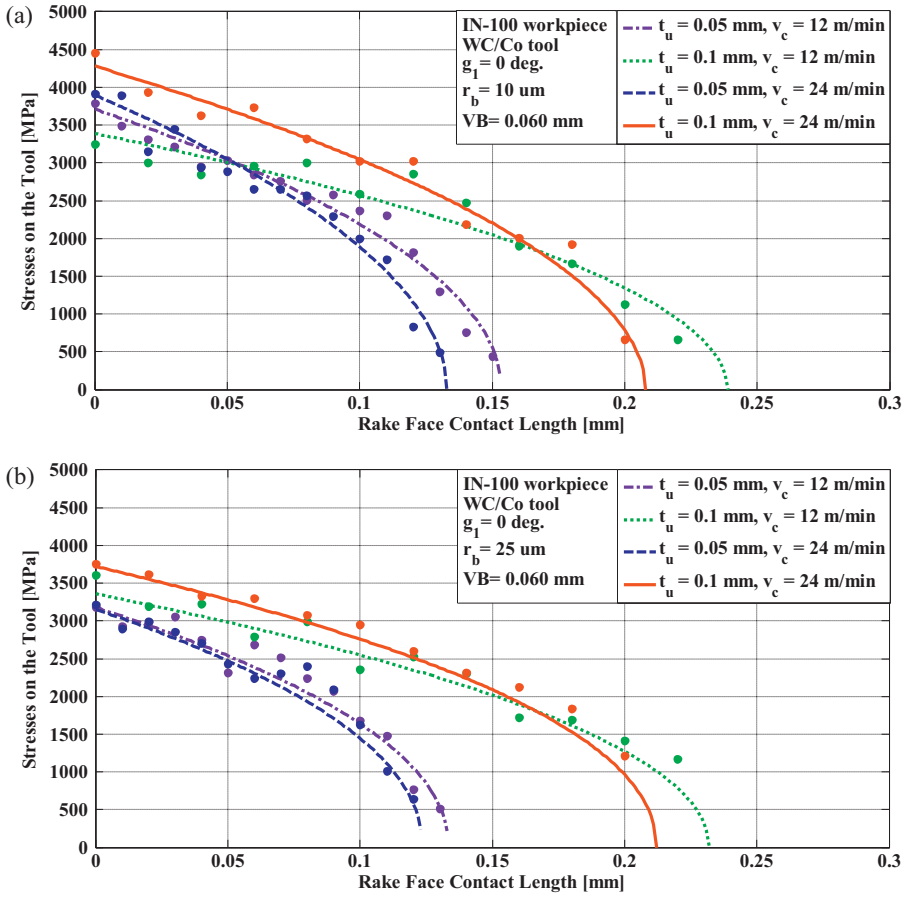


**Fig. 15.** Effect of $t_u$ and $v_c$ on tool rake face normal stress distributions for machining IN-100.

conditions, while the maximum normal and shear stresses on the edge face varied substantially. It was observed that with increasing edge radius, cutting speed, feed, and rake angle, maximum normal and shear stresses increased. Stagnation angle was found to be mostly dependent on tool edge radius, and with increasing edge radius from $r_\beta = 10$ to 25 μm, stagnation angle was found to increase from $\gamma_s = 10–15^\circ$ to $\gamma_s = 40–45^\circ$. However, tool wear was considered to be constant ($VB = 60$ μm) in all conditions, which means that these simulations represent the values after a certain and similar tool wear amount, regardless of cutting time or distance. Other process parameters did not affect the stagnation angle significantly.

### 5.3. Validation of titanium-based alloy (Ti-64) machining data

Stress distribution based validation studies have also been conducted to compare tool stresses calculated from friction determination method and FE-based simulation resultant stress fields for machining Ti-6Al-4V.

FE simulation results for the titanium alloy Ti-6Al-4V can be found in Table 7. The simulations were run for two different sets of experimentation. For higher cutting speed ($v_c = 120$ m/min), the experimental results were received from the orthogonal cutting tests conducted in (Özel et al., 2010). The experimental results for lower cutting speed ($v_c = 70$ m/min) were extracted from the orthogonal cutting test results in (Wyen and Wegener, 2010). In both experiment sets, uncoated tungsten carbide (WC) tools were used. Three different rake angles ($\gamma_1 = 0^\circ, 5^\circ$, and $10^\circ$), three different cutting edge radii ($r_\beta = 10$, 20 and 30 μm), two different cutting speeds ($v_c = 70$ and 120 m/min), and three different uncut chip thickness ($t_u = 0.05$, 0.06 and 0.1 mm) were used. However, the intention was to make the low feed values as close to each other as possible, as the two different measurement sets did not have equivalent lower values of uncut chip thickness. The two low values are very close to each other, and the difference in the effect can be assumed statistically non-significant. This way, it is possible to compare low feed (0.05–0.06 mm) to high feed (0.1 mm) results. In total, it is possible to see the effect of all four cutting parameters in 8 experiments/simulations.

FE-based simulations for the same 8 conditions were run with DEFORM-2D FEM software. Fig. 25b shows a representative stress field, and Fig. 25a shows a sample comparison between the stress fields extracted from the FE-based simulations and the stress fields obtained from the friction determination method. It was observed from the results that in the cutting speed direction (hoop or tangential stress in orthogonal cutting), tensile machining-induced stress values became less apparent with increasing feed and rake angle values, but more apparent with increasing cutting edge radius. Tool stresses became more compressive with increasing feed, while the other parameters did not have significant effects.

The influence of tool rake angle, edge radius and cutting conditions has also been investigated for machining Ti-6Al-4V titanium alloy. These results are presented in Figs. 26–29 where all normal stresses are compressive. In the feed direction (longitudinal in orthogonal cutting), machining-induced stresses on the workpiece did not seem to change much with any of the parameters, but tool stresses were observed to become more compressive with increasing feed and decreasing edge radius values. In the depth

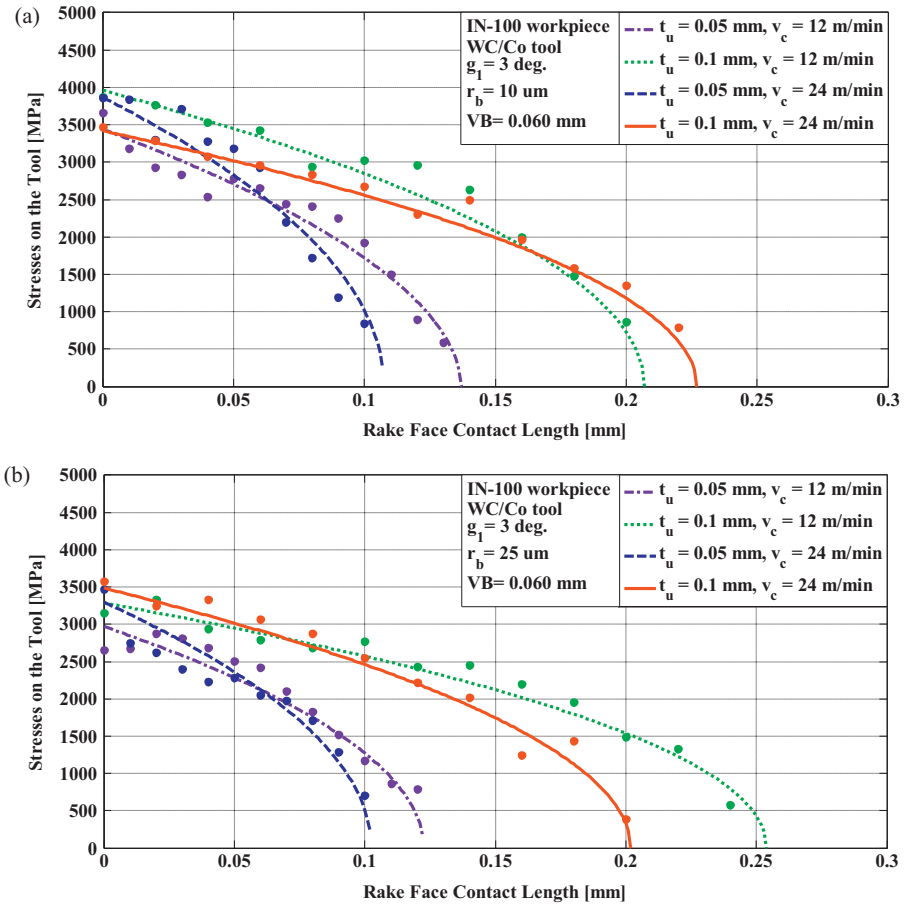


**Fig. 16.** Effect of $t_u$ and $v_c$ on tool rake face normal stress distributions for machining IN-100.

of cut direction (radial direction in orthogonal cutting), increasing feed was found to increase the compressive stresses on the tool, but no other significant effects were observed.

It can be also observed from Table 6 that none of the parameters had any significant effect on the friction coefficients, and the rake face friction coefficients were found to be around $\mu_1 = 0.6$ for all the parameters used. The flank face friction coefficient was also constant around $\mu_2 = 0.51$, except for the highest cutting edge radius ($r_\beta = 30$ μm), where it dropped slightly to $\mu_2 = 0.45$–$0.49$. Maximum shear stress on the rake face was found to increase with feed, edge radius, and rake angle, and also significantly with cutting speed. The magnitude of maximum normal and shear stresses on the edge face both increased with increasing feed, decreased with edge radius, and stayed similar with changing rake angle. Increasing cutting speed decreased the maximum normal stress on the edge face, while not affecting significantly the maximum shear stress on the edge face. The stagnation angle was found to decrease slightly with increasing feed, and not change significantly with cutting speed or

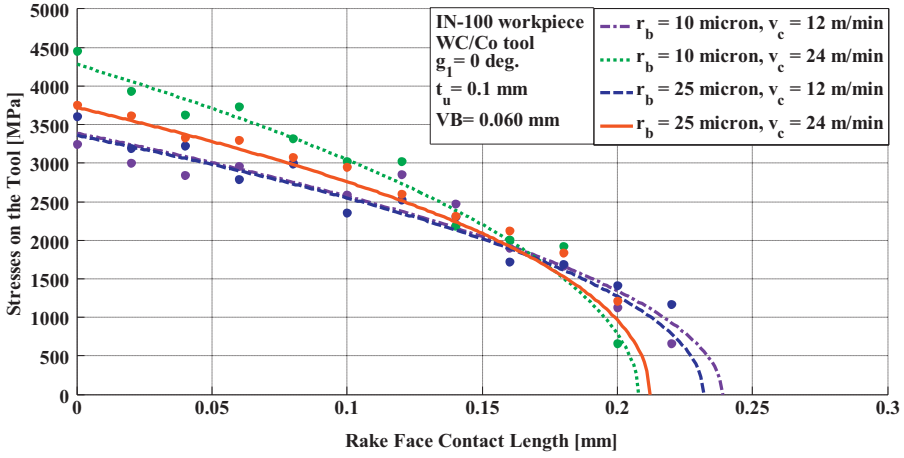


**Fig. 17.** Effect of $r_\beta$ and $v_c$ on tool rake face normal stress distributions for machining IN-100.

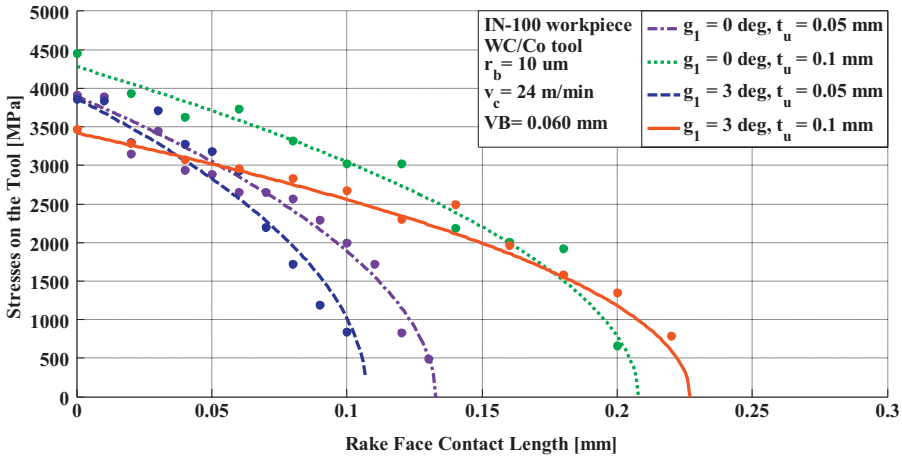


**Fig. 18.** Effect of $\gamma_1$ and $t_u$ on tool rake face normal stress distributions for machining IN-100.

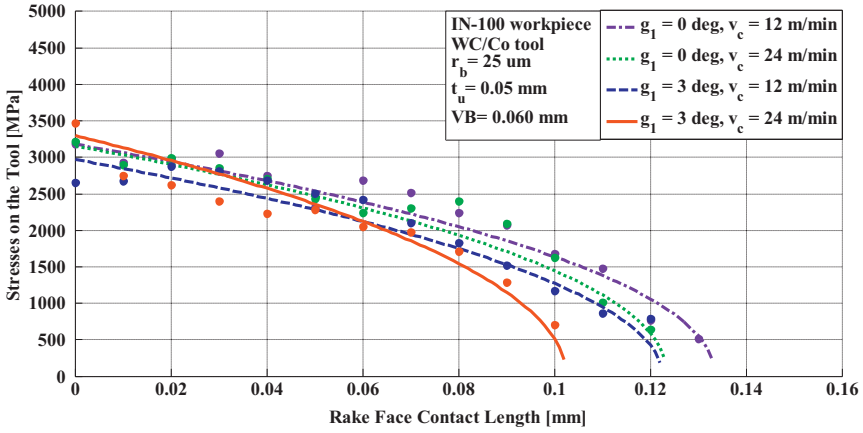


**Fig. 19.** Effect of $\gamma_1$ and $v_c$ on tool rake face normal stress distributions for machining IN-100.

the rake angle. As with the nickel-based alloy IN-100, the stagnation angle during machining the titanium alloy Ti-64 also depended heavily on edge radius, and with edge radius increasing from $r_\beta = 10$ to 20 and 30 μm, stagnation angle increased from around $\gamma_s = 10^\circ$ to $\gamma_s = 27$ and 45°, respectively.

## 6. Discussions

As it can be observed from the Figs. 30 and 31, the findings of these analyses show that the forces and stresses on the tool depend heavily on the machining parameters. Fig. 30 shows for the

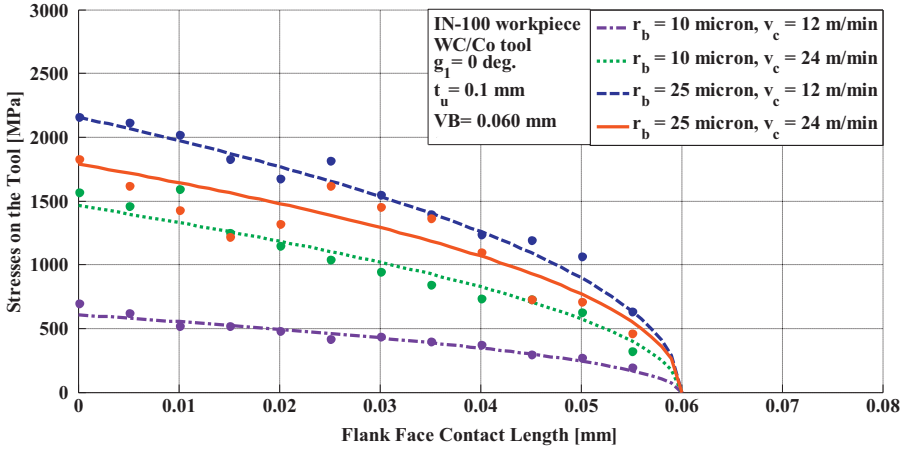


**Fig. 20.** Effect of $r_\beta$ and $v_c$ on tool flank face normal stress distributions for machining IN-100.

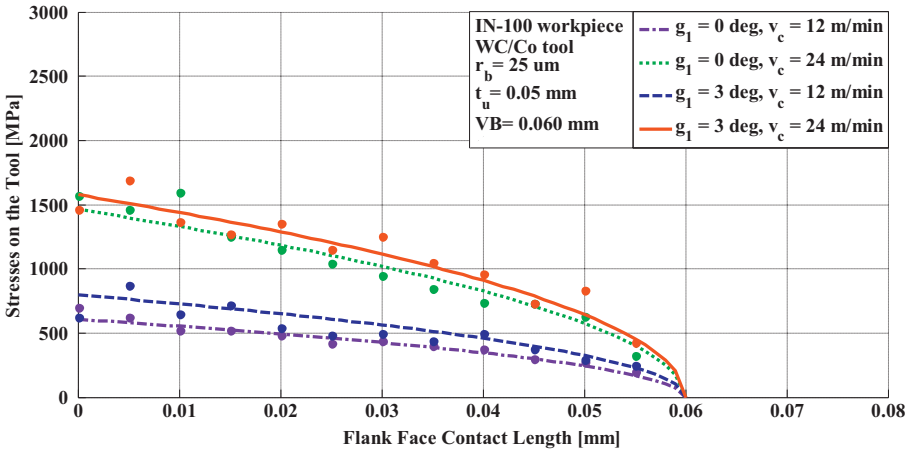


**Fig. 21.** Effect of $\gamma_1$ and $v_c$ on tool flank face normal stress distributions for machining IN-100.

nickel-based alloy IN-100 that the change of rake angle from $\gamma_1 = 0$ to 3° mostly increases the cutting forces while decreasing the thrust forces, where its effect on the maximum stress components on the tool rake and flank faces is negligible. Cutting edge radius and cutting speed do not seem to affect the force components significantly, whereas with increasing cutting edge radius from $r_\beta = 10$ to 25 μm, flank face stresses increase significantly, as more load is applied on the flank face. This results in a decrease in the rake face stresses as expected. With increasing cutting speed, flank and rake face stresses increase slightly. The effect of feed on stresses is small, whereas an increase in the uncut chip thickness from $t_u = 0.05$ to 0.1 mm immensely affects the force components as the load on the tool is doubled.

For the titanium alloy Ti-64, Fig. 31 shows that the effect of uncut chip thickness from a low amount ($t_u = 0.05$–$0.06$ mm) to a higher amount ($t_u = 0.1$ mm) reflects a similar result on the force components, particularly the cutting force. The effect of cutting edge

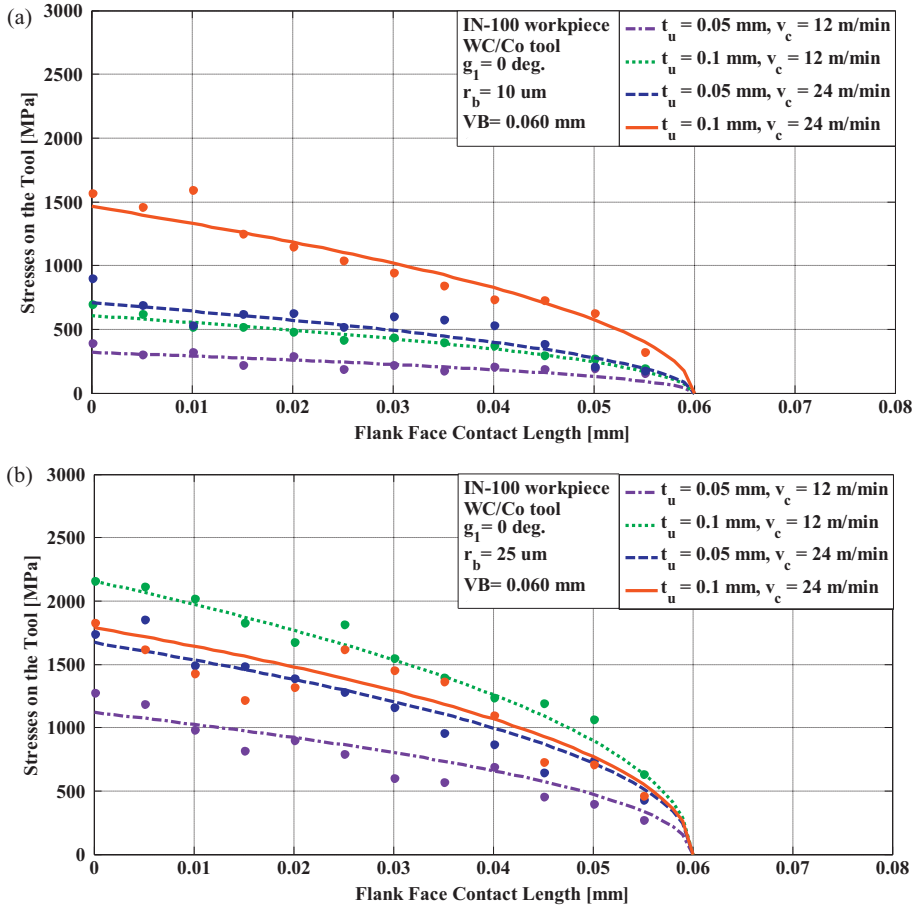


**Fig. 22.** Effect of $t_u$ and $v_c$ on tool flank normal face stress distributions for machining IN-100.

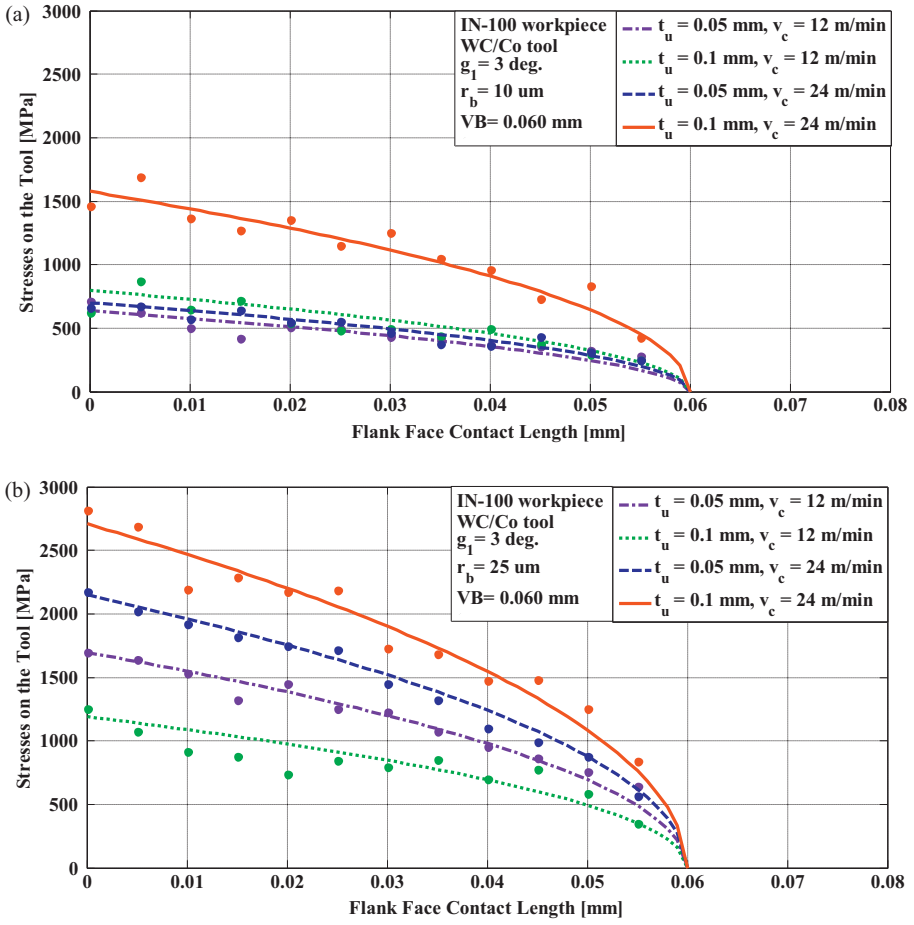


**Fig. 23.** Effect of $t_u$ and $v_c$ on tool flank face normal stress distributions for machining IN-100.

radius is reversed on this material, mostly due to the high rake angle in these conditions ($\gamma_1 = 10^\circ$), as well as the low width of cut, which decreases the total load significantly. It can also be observed that with increasing cutting speed from $v_c = 70$ to 120 m/min, both force components decrease. Finally, it is also seen that with increasing rake angle from $\gamma_1 = 0$ to 5°, as well as with increasing cutting speed from $v_c = 70$ to 120 m/min, rake face stresses increase a noteworthy amount.

On the other hand, the stagnation point angles summarized in Tables 6 and 7 have been utilized and the effects of the ratio of cutting edge radius between uncut chip thickness ($r_\beta/t_u$) on the location of stagnation point in machining Ti-6Al-4V and IN-100 have been compared with the findings summarized from literature as shown in Fig. 32.

It was observed that similar to the literature, the stagnation point angle increases with the increasing cutting edge radius to

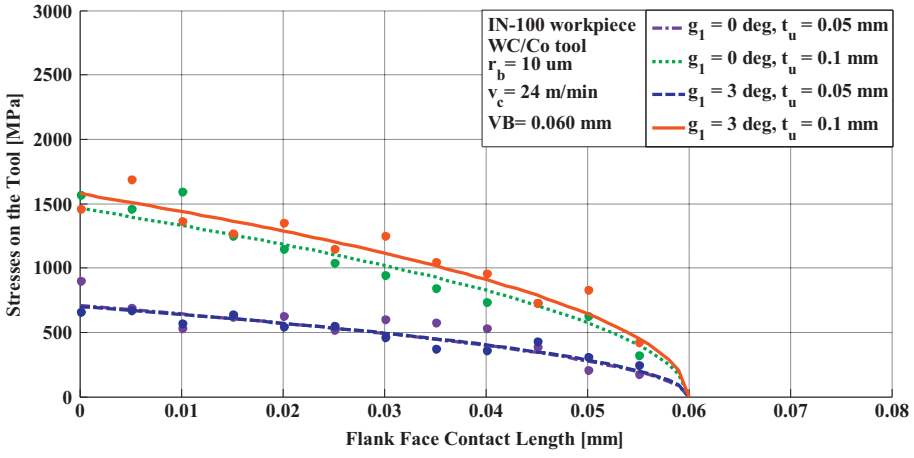


**Fig. 24.** Effect of $\gamma_1$ and $t_u$ on tool flank face normal stress distributions for machining IN-100.

**Table 7**
Search algorithm results compared to orthogonal cutting results for Ti-6Al-4V.

| Experimental | | | | | FEM Results | | | | | | | FDM Results | | | | | |
|---|---|---|---|---|---|---|---|---|---|---|---|---|---|---|---|---|---|
| $r_\beta$ [μm] | $v_c$ [m/min] | $t_u$ [mm] | $b$ [mm] | $F_t/b$ [N/mm] | $F_c/b$ [N/mm] | $\sigma_{1max}$ [MPa] | $n$ | $\sigma_{3max}$ [MPa] | $m$ | $l_c/t_u$ | $l_p/t_u$ | $F_t/b$ [N/mm] | $F_c/b$ [N/mm] | $\mu_1$ | $\mu_2$ | $\tau_{1max}$ [MPa] | $\bar{\sigma}_2$ [MPa] | $\bar{\tau}_2$ [MPa] | $\gamma_s$ [°] |
| $\gamma_1 = 0°$ | | | | | | | | | | | | | | | | | | | |
| 10 | 120 | 0.05 | 5 | 51 | 104 | 1974 | 0.45 | 693 | 0.35 | 1.37 | 0.35 | 59 | 99 | 0.60 | 0.51 | 1013 | 544 | −555 | 11.3 |
| 10 | 120 | 0.1 | 5 | 80 | 189 | 2524 | 0.55 | 1485 | 0.34 | 1.36 | 0.41 | 93 | 195 | 0.59 | 0.51 | 1215 | 1167 | −1189 | 8.8 |
| $\gamma_1 = 5°$ | | | | | | | | | | | | | | | | | | | |
| 10 | 120 | 0.05 | 5 | 48 | 99 | 3247 | 0.52 | 611 | 0.32 | 1.41 | 0.52 | 49 | 104 | 0.60 | 0.52 | 1498 | 483 | −489 | 12.0 |
| 10 | 120 | 0.1 | 5 | 67 | 180 | 3701 | 0.52 | 1349 | 0.32 | 1.38 | 0.57 | 65 | 189 | 0.60 | 0.52 | 1645 | 1066 | −1078 | 8.6 |
| $\gamma_1 = 10°$ | | | | | | | | | | | | | | | | | | | |
| 20 | 70 | 0.06 | 2 | 75 | 128 | 1566 | 0.47 | 861 | 0.39 | 1.34 | 0.36 | 75 | 124 | 0.59 | 0.51 | 793 | 908 | −324 | 28.1 |
| 20 | 70 | 0.1 | 2 | 83 | 188 | 1921 | 0.49 | 1301 | 0.40 | 1.31 | 0.33 | 94 | 189 | 0.58 | 0.51 | 974 | 1378 | −487 | 25.8 |
| 30 | 70 | 0.06 | 2 | 110 | 139 | 1831 | 0.48 | 659 | 0.32 | 1.44 | 0.45 | 88 | 150 | 0.59 | 0.45 | 897 | 708 | −145 | 45.3 |
| 30 | 70 | 0.1 | 2 | 113 | 191 | 2342 | 0.45 | 891 | 0.31 | 1.40 | 0.43 | 123 | 207 | 0.59 | 0.49 | 1162 | 958 | −195 | 45.0 |

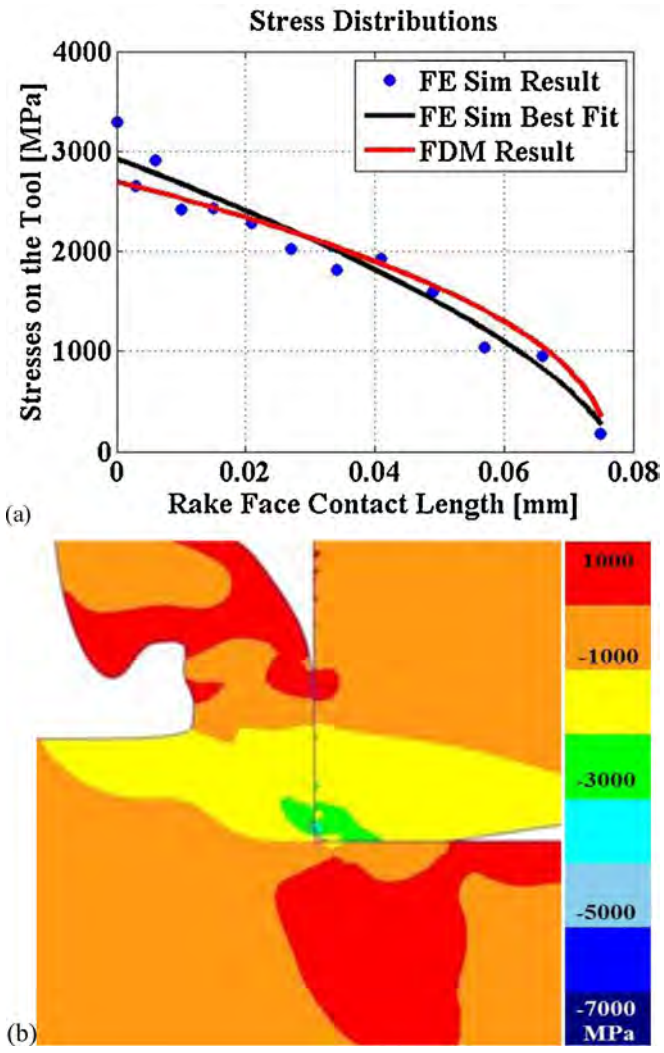


**Fig. 25.** Comparison of Ti-6Al-4V (a) predicted compressive normal stresses on the tool and (b) FE-based simulation stress distribution ($v_c$ = 120 m/min, $t_u$ = 0.05 mm, $r_\beta$ = 10 μm, $\gamma_1$ = 5°).

uncut chip thickness ratio. While stagnation point location is not much affected when an undeformed chip thickness greater than tool edge radius is taken, the stagnation point location is influenced by the size of the edge radius at a constant undeformed chip thickness condition. The trend lines obtained for this increase are more aligned with the work presented by Kishawy et al. (2006) for cutting AISI 4140 steel. The study by Woon et al. (2008) shows a stagnation angle mostly not affected from the uncut chip thickness in micro-cutting of AISI 1045 steel while Fang and Xiong (2008) reports higher stagnation angles and an increase for increasing edge radius to uncut chip thickness ratio in cutting AL 2024 and Copper 330.

These observations confirm that as the edge radius becomes larger or uncut chip thickness gets smaller, there will be a longer contact region around the round edge from the stagnation point into the flank face increasing the tool wear rate in machining of Ti-6Al-4V titanium and IN-100 nickel-based alloys. It should be noted that there exist some prediction error in this proposed approach which is based on calculated stress distributions along the tool edge radius.

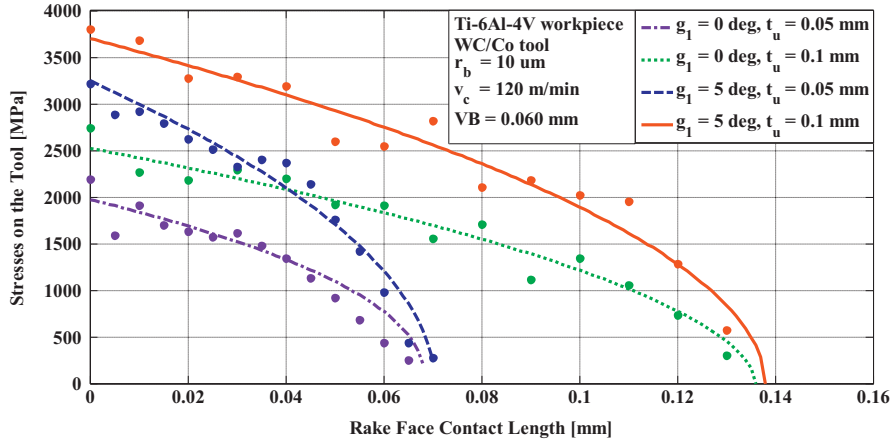


**Fig. 26.** Effect of $\gamma_1$ and $t_u$ on tool rake face normal stress distributions for machining Ti-6Al-4V.

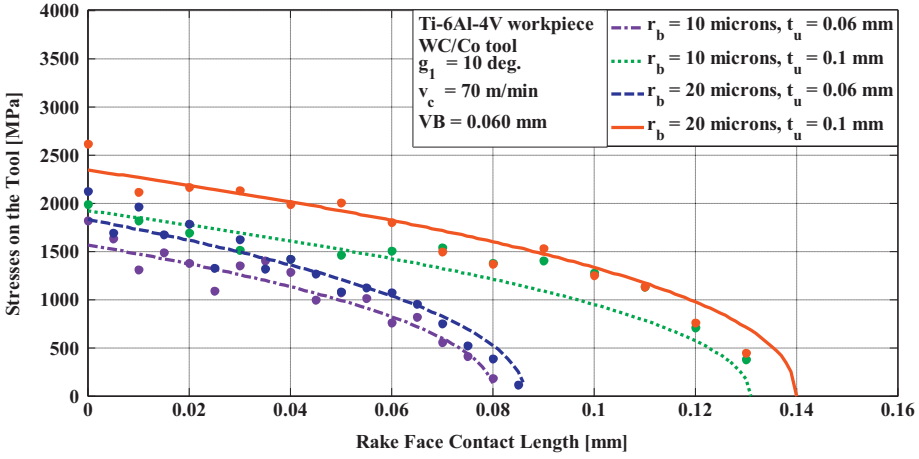


**Fig. 27.** Effect of $r_\beta$ and $t_u$ on tool rake face normal stress distributions for machining Ti-6Al-4V.

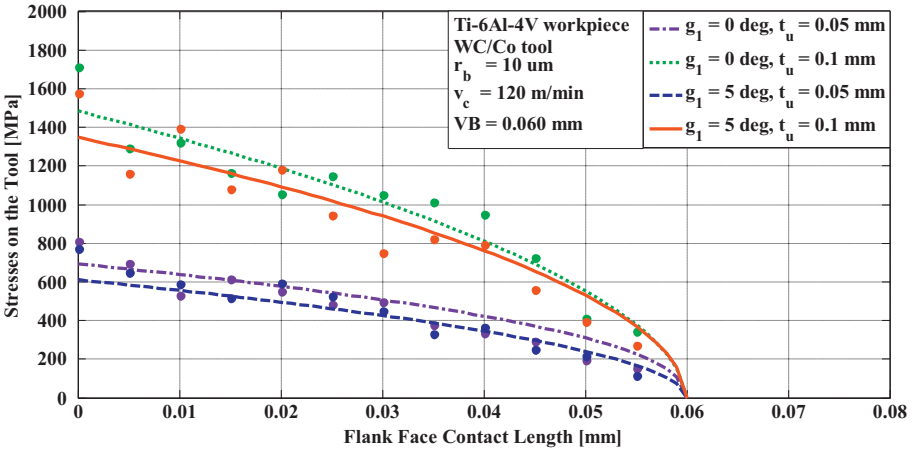


**Fig. 28.** Effect of $\gamma_1$ and $t_u$ on tool flank face normal stress distributions for machining Ti-6Al-4V.

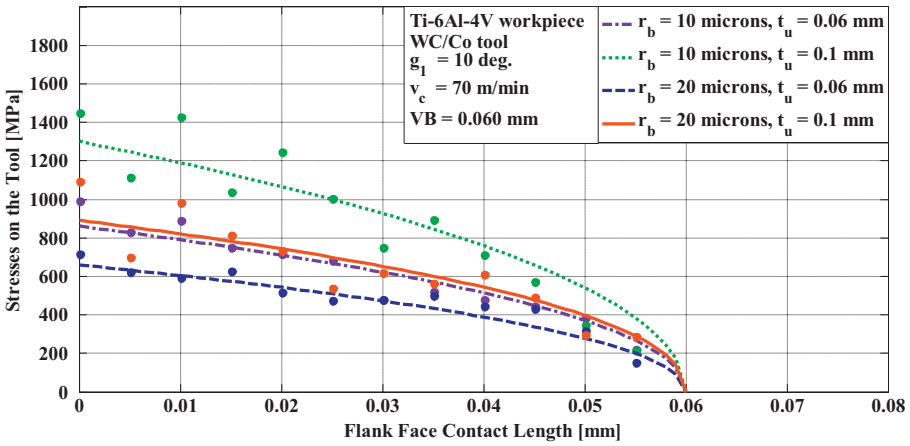


**Fig. 29.** Effect of $r_\beta$ and $t_u$ on tool flank face normal stress distributions for machining Ti-6Al-4V.

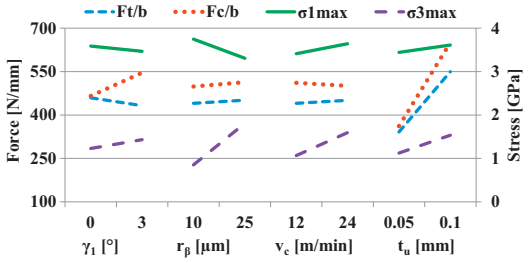


**Fig. 30.** Effects of tool geometry and cutting conditions on tool forces and normal stresses (IN-100).

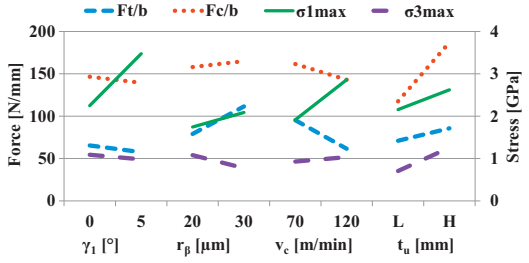


**Fig. 31.** Effects of tool geometry and cutting conditions on tool forces and normal stresses (Ti-6Al-4V).

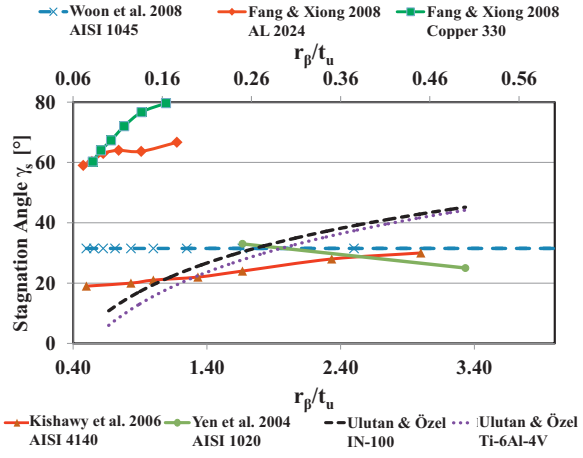


**Fig. 32.** Effects of tool geometry and cutting conditions on stagnation point angle.

## 7. Conclusions

Titanium and nickel-based alloys possess significant difficulty for machining processes. Since friction plays an important role in machining processes, especially during dry machining, and is an important input to the modeling studies, this work aims at introducing a new methodology to determine tool friction and related stress distribution parameters during machining Ti-6Al-4V titanium and IN-100 nickel-based alloys.

For this methodology, uncoated tools made with tungsten carbide (WC/Co) are considered. Orthogonal cutting tests have been utilized for measured cutting forces that are obtained at various tool rake angles, edge radii, cutting speeds, and feed. Two different solutions were introduced, one with unworn tool geometry, and the other one with worn tool geometry, and the results were reflected to show the tool friction and related stress distribution parameters under different cutting parameters and flank wear conditions. It was found that while the friction coefficients did not depend on most of the cutting parameters in machining titanium and nickel-based alloys, they changed with changing workpiece material, and slightly with cutting edge geometry. However, tool stress distribution parameters are largely affected by tool geometry and slightly affected by cutting conditions. Furthermore, stress distribution solution over the round edge tool also provided stagnation point location as validated with the work by other researchers.

This methodology can be used to determine tool friction characteristics for practical purposes and also as an input to the FEM based modeling and simulations studies. Furthermore, the methodology also offers to be expanded to other materials and cutting parameters via gathering of more orthogonal cutting tests.

## Acknowledgements

The financial support provided by the National Science Foundation (grant number CMMI-1130780), support for DEFORM software by SFTC, Ohio, USA are gratefully acknowledged.

## References

Albrecht, P., 1960. New developments in the theory of the metal-cutting process. Transactions of the ASME—Journal of Engineering for Industry, 348–358.

Arrazola, P., Meslin, F., 2002. A Technique for the Identification of Friction at Tool/Chip Interface during Machining. In: Proceedings of the Second Asia International Conference on Tribology.

Arrazola, P., Özel, T., 2010. Investigations on the effects of friction modeling in finite element simulation of machining. International Journal of Mechanical Sciences 52, 31–42.

Arrazola, P., Ugarte, D., Domínguez, X., 2008. A new approach for the friction identification during machining through the use of finite element modeling. International Journal of Machine Tools & Manufacture 48, 173–183.

Bonnet, C., Valiorgue, F., Rech, J., Claudin, C., Hamdi, H., Bergheau, J.M., Gilles, P., 2008. Identification of a friction model—application to the context of dry cutting of an AISI 316L austenitic stainless steel with a TiN coated carbide tool. International Journal of Machine Tools & Manufacture 48, 1211–1223.

Childs, T.H.C, 2006a. Friction modeling in metal cutting. Wear 260, 310–318.

Childs, T.H.C., 2006b. Numerical experiments on the influence of material and other variables on plane strain continuous chip formation in metal machining. International Journal of Mechanical Sciences 48, 307–322.

Fang, N., 2003. Slip-line modeling of machining with a rounded-edge tool—Part II: analysis of the size effect and the shear strain-rate. Journal of the Mechanics and Physics of Solids 51, 743–762.

Fang, N., Xiong, L.S., 2008. Determination of friction and material-flow boundary conditions on the tool round cutting edge. Transactions of NAMRI/SME 36, 413–420.

Hedenqvist, P., Olsson, M., 1991. Sliding wear testing of coated cutting tool materials. Tribology International 23 (3), 143–150.

Kishawy, H.A., Haglund, A.J., Deiab, I.M., 2006. An analysis of machining with honed tools using ALE finite element model: ploughing force and minimum chip thickness. Transactions of NAMRI/SME 34, 277–284.

Molinari, A., Cheriguene, R., Miguelez, H., 2011. Numerical and analytical modeling of orthogonal cutting: the link between local variables and global contact characteristics. International Journal of Mechanical Sciences 53, 183–206.

Moufki, A., Molinari, A., Dudzinski, D., 1998. Modelling of orthogonal cutting with a temperature dependent friction law. Journal of the Mechanics and Physics of Solids 46 (10), 2103–2138.

Olsson, M., Soderberg, S., Jacobson, S., Hogmark, S., 1989. Simulation of cutting tool wear by a modified pin-on-disc test. International Journal of Machine Tools & Manufacture 29 (3), 377–390.

Özel, T., 2006. The influence of friction models on finite element simulations of machining. International Journal of Machine Tools & Manufacture 46, 518–530.

Özel, T., 2009. Experimental and finite element investigations on the influence of tool edge radius in machining nickel-based alloy. In: CD Proceedings of 2009 ASME International Conference on Manufacturing Science and Engineering, Paper No. 84362, October 5–7, Lafayette, IN, USA.

Özel, T., Sima, M., Srivastava, A.K., Kaftanoglu, B., 2010. Investigations on the effects of multi-layered coated inserts in machining Ti-6Al-4V alloy with experiments and finite element simulations. CIRP Annals—Manufacturing Technology 59, 77–82.

Özlü, E., Budak, E., Molinari, A., 2009. Analytical and experimental investigation of rake contact and friction behavior in metal cutting. International Journal of Machine Tools & Manufacture 49 (11), 865–875.

Sutter, G., Molinari, A., 2005. Analysis of the cutting force components and friction in high speed machining. Journal of Manufacturing Science and Engineering 127, 245–250.

Woon, K.S., Rahman, M., Neo, K.S., Liu, K., 2008. The effect of tool edge radius on the contact phenomenon of tool-based micromachining. International Journal of Machine Tools & Manufacture 48, 1395–1407.

Wyen, C.-F, Wegener, K., 2010. Influence of cutting edge radius on cutting forces in machining titanium. CIRP Annals—Manufacturing Technology 59, 93–96.

Yen, Y.C., Jain, A., Altan, T., 2004. A finite element analysis of orthogonal machining using different tool edge geometries. Journal of Materials Processing Technology 146, 72–81.

Zorev, N.N., 1963. Interrelationship between shear processes occurring along tool faces and on shear plane in metal cutting. In: International Research in Production Engineering, Proceedings of the International Production Engineering Research Conference, pp. 42–49.